SAND2022-10400J

2D imaging of absolute methyl concentrations in nanosecond pulsed plasma by photo-fragmentation laser-induced fluorescence

Dirk van den Bekerom[1], Caleb Richards[2], Erxiong Huang[1], Igor Adamovich[2], and Jonathan H. Frank[1]

[1]*Combustion Research Facility, Sandia National Laboratories, 7011 East Ave, Livermore, CA 94550 USA*

[2]*Department of Mechanical and Aerospace Engineering, The Ohio State University, 201 W 19th Ave, Columbus, OH 43210 USA*

Corresponding author email: jhfrank@sandia.gov

Abstract

The methyl radical plays a central role in plasma-assisted hydrocarbon chemistry but is challenging to detect due to its high reactivity and strongly pre-dissociative electronically excited states. We report the development of a photo-fragmentation laser-induced fluorescence (PF-LIF) diagnostic for quantitative 2D imaging of methyl profiles in a plasma. This technique provides temporally and spatially resolved measurements of local methyl distributions, including in near-surface regions that are important for plasma-surface interactions such as plasma-assisted catalysis. The technique relies on photo-dissociation of methyl by the fifth harmonic of a Nd:YAG laser at 212.8 nm to produce CH fragments. These photofragments are then detected with LIF imaging by exciting a transition in the B-X(0,0) band of CH with a second laser at 390 nm. Fluorescence from the overlapping A-X(0,0), A-X(1,1), and B-X(0,1) bands of CH is detected near 430 nm with the A-state populated by collisional B-A electronic energy transfer. This non-resonant detection scheme enables interrogation close to a surface. The PF-LIF diagnostic is calibrated by producing a known amount of methyl through photo-dissociation of acetone vapor in a calibration gas mixture. We demonstrate PF-LIF imaging of methyl production in methane-containing nanosecond pulsed plasmas impinging on dielectric surfaces. Absolute calibration of the diagnostic is demonstrated in a diffuse, plane-to-plane discharge. Measured profiles show a relatively uniform distribution of up to 30 ppm of methyl. Relative methyl measurements in a filamentary plane-to-plane discharge and a plasma jet reveal highly localized intense production of methyl. The utility of the PF-LIF technique is further demonstrated by combining methyl measurements with formaldehyde LIF imaging to capture spatiotemporal correlations between methyl and formaldehyde, which is an important intermediate species in plasma-assisted oxidative coupling of methane.

1. Introduction

Methyl is a key radical in plasma-assisted hydrocarbon chemistry, and quantitative in-situ imaging measurements of methyl are needed to improve fundamental understanding for a broad range of plasma applications. Methyl is particularly important in methane chemistry because it is produced in the first step of methane dehydrogenation. For example, in plasma-assisted methane combustion, methyl is formed by collisions of methane with OH, electrons, O, and H, and its subsequent oxidation is central to the formation of products and intermediate species [Ju2015]. Methyl radicals are also believed to be a dominant growth precursor in plasma-assisted chemical vapor deposition (CVD) of diamond films [Goodwin2018]. Methyl is recognized as a key intermediate in plasma catalytic oxidation of methane to methanol [Li2021] and plays an important role in non-oxidative coupling of methane in the plasma volume, such as in microwave plasmas [Minea2018]. It is also under study as a means of functionalizing graphene sheets [Pei2010].

Plasma-catalysis coupling of methane is a promising alternative to conventional thermal catalysis for conversion of methane to oxygenates or higher value hydrocarbon species, and its importance is recognized in plasma research roadmaps [Adamovich2017, Bogaerts2020]. The generation of highly reactive species in the plasma can facilitate chemical conversion at low temperatures, which reduces energy use, coking of catalyst surfaces, and the undesirable complete oxidation of products in the case of oxidative coupling of methane (OCM). Plasma coupled catalysts are experiencing a surge in interest, but most research is limited to measurements of the products in the effluent. The high reactivity of methyl makes it difficult or even impossible to detect in the effluent of a reactor. While surface species on the plasma coupled catalyst are the subject of great interest [Somers2012, Neyts2016], only a few authors have reported direct in-situ measurements of adsorbed species to date [Whitehead2016, Barakat2014, Stere 2015]. Development of in-situ, time resolved diagnostics is needed to answer fundamental questions about the interaction between plasma and catalyst, for example whether methyl chemistry is dominated by Langmuir-Hinshelwood or Eley-Rideal type reactions [Chawdhury2021]. In effect, an imaging diagnostic capable of probing the plasma and near-surface region of the catalyst is highly desirable.

Detection of methyl in chemically reacting gas-phase systems is most often performed using techniques that provide single-point or line-of-sight measurements, such as absorption [Sherer1997], resonance-enhanced multi-photon ionization (REMPI) [Meier1987, Wu2011], mass spectrometry [McIlroy2000, Taatjes2008, Zhou2021], and degenerate four-wave mixing (DFWM) [Sick1995]. Two-dimensional imaging measurements are needed to determine the spatial distribution of methyl. Although planar laser-induced fluorescence is widely used for 2D imaging of reactive species such as OH, NO, CH, and CH_2O in both flames and plasmas [Hanson1988, Kaminski2002, Kohse-Hoinghaus2005, Sainct2014, Schmidt2014, Ouaras2018, Frank2021, vandenBekerom2021], strong pre-dissociation of the electronically excited states of methyl precludes the use of direct LIF detection schemes. However, pre-dissociation enables the use of photo-fragmentation techniques in which methyl is dissociated using laser photolysis and the resulting photofragments are detected. This approach has previously been demonstrated for qualitative imaging of methyl in flames. In studies of low-pressure premixed methane-air flames, Desgroux et al. noted that photo-dissociation of methyl at 205 nm produces CH_2 fragments, which are also photo-dissociated to produce electronically excited CH fragments [Desgroux1996]. Fluorescence emission from the excited CH radicals can be detected and is proportional to the initial CH_3 density, a process named laser photo-fragmentation induced fluorescence (LPIF). Subsequently, Li et al. demonstrated LPIF of methyl in atmospheric pressure methane-air flames using the fifth harmonic of a pulsed Nd:YAG laser at 212.8 nm with energies up to 15 mJ per pulse [Li2015], an increase in laser energy and associated signal level of an order of magnitude. Li et al. further improved the detection

sensitivity by combining photo-fragmentation of CH_3 with LIF of the CH photo-fragments for single-shot methyl imaging in a turbulent flame [Li2017], increasing signal levels by another order of magnitude. This approach is referred to as photo-fragmentation laser-induced fluorescence (PF-LIF) and has recently been used to study the structure of methyl distributions qualitatively in turbulent flames [Wan2021, Wan2022]. The actual increase in signal levels for PF-LIF depends on the conditions. However, another important advantage of PF-LIF is that the probe can be delayed with respect to the photo-fragmentation beam to eliminate interferences.

The present investigation builds on the previous qualitative imaging of methyl in flames in three ways: We demonstrate the CH_3 PF-LIF diagnostic technique in a plasma, employ a non-resonant detection scheme suitable for measurements near a surface, and provide an absolute calibration strategy for quantitative methyl measurements. For these demonstrations, we use an optically accessible plasma reactor that enables in-situ imaging of radicals, intermediates, and products as well as probing of plasma-surface interactions, such as plasma-assisted catalysis. Methyl measurements in a nanosecond pulsed plasma are presented for three different conditions: a diffuse, homogenous plane-to-plane discharge, a filamentary plane-to-plane discharge, and a plasma jet. The measurements in the homogenous plane-to-plane discharge yielded absolute methyl density, while the other two configurations yielded relative methyl measurements. We further demonstrate combined methyl PF-LIF and formaldehyde LIF imaging to highlight the potential for using multiple imaging measurements to provide a more complete picture of species distributions in methane plasma chemistry.

2. Experimental

2.1 Non-resonant PF-LIF

For the first step of methyl photo-fragmentation LIF, we use the fifth harmonic of a Nd:YAG laser at 212.8nm to photo-dissociate CH_3 to form CH radicals. The second step involves probing the CH photofragments using a suitable CH-LIF excitation-detection scheme. CH has three optically accessible electronic states (A, B, C), providing flexibility on the LIF excitation and detection schemes. All three have been used in calibrated LIF measurements [Tsujishita1993, Jacob1994, Luque1996-1, Luque1996-2, Luque1997, Luque2002, Juckmann1998, Bohm2005, Gibaud2005]. Typical schemes involve excitation in the A-X(0,0) band [Luque1996-1, Luque1996-2, Luque1997,Walsh1998, Gibaud2005] or B-X(0,0) band [Jacob1994, Luque1996-1, Luque1996-2, Luque1997] followed by resonant detection. Quantitative interpretation of the LIF signals requires knowledge of the local collisional quenching rate, which can be measured directly at low pressures [Luque1996-1, Luque1996-2, Luque1997, Juckmann1998, Bohm2005] or calculated [Walsh1998, Gibaud2005]. In certain environments, the pre-dissociated B(v'=1) state and C-state can be used to reduce sensitivity to collisional quenching [Tsujishita1993, Luque2002], but this may be at the cost of reduced LIF-signal intensity. At atmospheric pressure and above however, quenching of the C-state is again dominated by electronic quenching [Carter2014, Hammack2017]. The schemes discussed so far rely on resonant detection due to the highly diagonal nature of the three bands, making them unsuitable for detection close to a surface where a non-resonant detection scheme is needed.

The requirement of non-resonant detection imposes constraints on the possible detection schemes. A number of non-resonant CH-LIF schemes have been successfully applied, including excitation of A-X(1,0) and detection at A-X(0,0) and A-X(1,1) [Paul1994], and B-X(1,0) excitation and detection at B-X(0,0) and B-X(1,1) [Dilecce2010]. Due to the weak off-diagonal bands however, these non-resonant schemes result in lower LIF-signals.

For this work, we used a popular non-resonant scheme that is frequently used in flames, which relies on excitation in the B-X(0,0) band, followed by detection of fluorescence from the A-X(0,0) and A-X(1,1) bands, and to a lesser extent the B-X(0,1) band [Carter1998, Watson2002, Bergthorson2005, Tanahashi2005, Vagelopoulos2005]. This scheme makes use of the fact that the $B^2\Sigma^-(v'=0)$ and $A^2\Delta(v'=1)$ states are very nearly resonant, which results in collisionally induced electronic energy transfer (EET) between the two levels [Garland1985, Juckmann1998, Bohm2005, Li2007, Kiefer2008]. The electronic energy transfer enables a non-resonant scheme by pumping a B-X (0,0) transition and detecting fluorescence in the overlapping A-X(1,1) and A-X(0,0) bands, as shown schematically in figure 1. The EET rate was measured to be approximately 30% of the total B(v=0) removal rate [Garland1985], but since EET is a collisional quenching process, the precise rate depends on the collisional environment. The A(v=1) level in turn is coupled to the A(v=0) level through vibrational energy transfer (VET), with all levels eventually decaying to the X state by collisional quenching and radiative decay.

This scheme has been used for calibrated CH-LIF measurements in combustion environments by obtaining quenching rates directly from fluorescence decay rate measurements [Juckmann1998, Bohm2005]. However, collisional energy transfer between the B and A states is highly complex [Garland1985, Luque2000, Randall2000, Richmond2005], so determining quenching from decay rates may result in significant uncertainties in the fluorescence yield. Because the emission rates for the diagonal A-X transitions are approximately 20 times greater than that of the B-X(0,1) transition, the measured decay rate is principally that of the A(v=0) and A(v=1) states. As such, this procedure does not yield information on the B-X quenching rate.

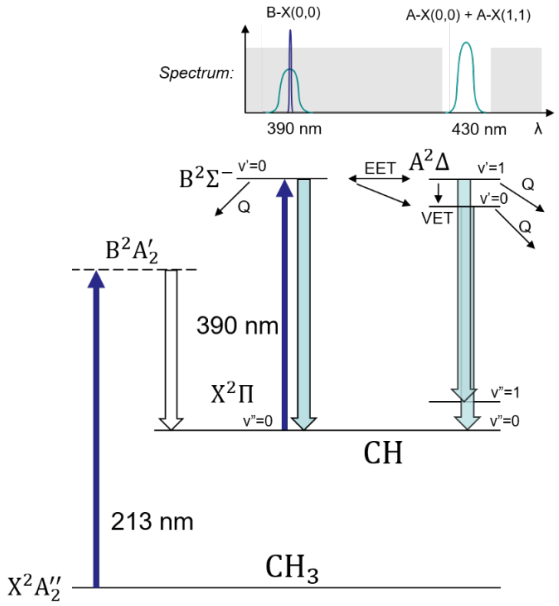

Figure 1: *PF-LIF scheme*

Absolute calibration of the diagnostic is further complicated by the fact that the methyl radical is highly reactive and cannot be introduced into the gas mixture but rather must be produced in-situ. We use photo-dissociation of acetone to produce a known and spatially well-defined methyl concentration. To record calibration images, we seed small quantities of Acetone into the reactant mixture.

Methyl selectivity is provided by the fact that most potentially interfering species have an absorption cross-section at least an order of magnitude lower [Li2017, Gardiner1987]. Moreover, interference could only be significant if the photofragmentation produces CH, which precludes major species such as CO_2, O_2, or H_2O. As suggested by Li et al., CH_2 is likely one of the main interfering species [Li2017].

In the afterglow of a plasma discharge, CH_2 could be present in significant quantities. The extent of interference depends on the ratios of CH_3 and CH_2 densities, absorption cross-sections, and quantum yields. At 212.8 nm, the absorption cross-section of CH_3 at 294 K is approximately 5 times larger than that of CH_2; $6.0 \cdot 10^{-18}$ cm^2 vs. $1.2 \cdot 10^{-18}$ cm^2, respectively [Cameron2002, Kroes1993]. The wavelength dependence of these cross-sections suggests that the ratio could be increased to a factor of approximately 80 by exciting methyl at 216.4 nm, which corresponds to the center of a strong CH_3 absorption peak. This would significantly improve the specificity of the methyl PF-LIF diagnostic at room temperature. For

higher temperature applications, the difference in the cross-sections at 212.8 nm and 216.4 nm may be less pronounced than at 294 K [Oehlschlaeger2005].

Despite the reasonably good specificity at 212.8 nm, CH_2 interference cannot be ruled out unless the CH_2 density can be shown to be less than or equal to that of CH_3. Measurements in methane RF-discharges using threshold ionization mass-spectrometry found an order of magnitude less CH_2 than CH_3 [Sugai1990], and a similar ratio was observed in microwave discharges [Jauberteau1997]. Numerical kinetic modelling supports these findings in microwave discharges [Yoon2002] and suggests that the difference could be even larger in oxygen containing RF-discharges, where CH_2 densities are predicted to be 2 - 3 orders of magnitude smaller than CH_3 densities [Moeller2006].

We are not aware of studies on relative CH_2 and CH_3 densities that are directly relevant to the ns-pulse DBD-plasmas in the present experiments, but a qualitative picture can be obtained by comparing the threshold energies and branching ratios of kinetic pathways producing these radicals. Considering the threshold energy for electron impact dissociation reactions, we find a threshold energy of 8.8 eV for the reactions from CH_4 to CH_3, and energies of 9.4 eV and 9.5 eV for reactions that produce CH_2 from CH_4 and CH_3, respectively [Janev2002]. Based on these differences in threshold energies, we could expect the production rate of CH_3 to be higher than that of CH_2. Reaction path flux analysis of reactions in the context of plasma assisted oxidation of methane in ns-DBDs indicates that 14% of the reacting methane is converted directly to CH_3 by electron impact, whereas only 10% is converted to CH_2 (either directly or through the CH_3^+ intermediate) [Lefkowitz2015]. That same study indicates that CH_3 production is also significantly favored by hydrogen abstraction reactions of CH_4 with OH and $O(^1D)$, which could account for approximately 50% of methane consumption.

Other studies exclude CH_2 production by electron impact entirely, suggesting that electron impact produces exclusively CH_3 [Togai2016]. This picture changes in the presence of argon, since electronically excited metastable argon (11.5 eV) is sufficiently energetic to dissociate methane upon collision [Balamuta1983]. Methane dissociated in this way favors the formation of CH_2 (62%) over other pathways, including one that results in CH_3 formation. While the gas mixtures in the present work don't include any argon, we cannot rule out the existence of a similar pathway for electronically excited He, which has an energy of 19.8 eV.

2.2 Experimental layout

The plasma apparatus is shown in Figure 2 and consists of a nanosecond pulsed plasma source that is integrated into a quartz cell, which enables control of the gas composition and pressure as well as the temperature of a heated surface that interacts with the plasma. The quartz discharge cell is a six-arm cross with 50.8 mm diameter arms. The four arms in the horizontal plane are covered by fused silica windows. Gas is introduced through a 12.7 mm diameter inlet, and a vacuum pump is connected to a 12.7 mm diameter outlet. The pressure is maintained at set values between 60-600 Torr by a PID-controller that operates a butterfly valve.

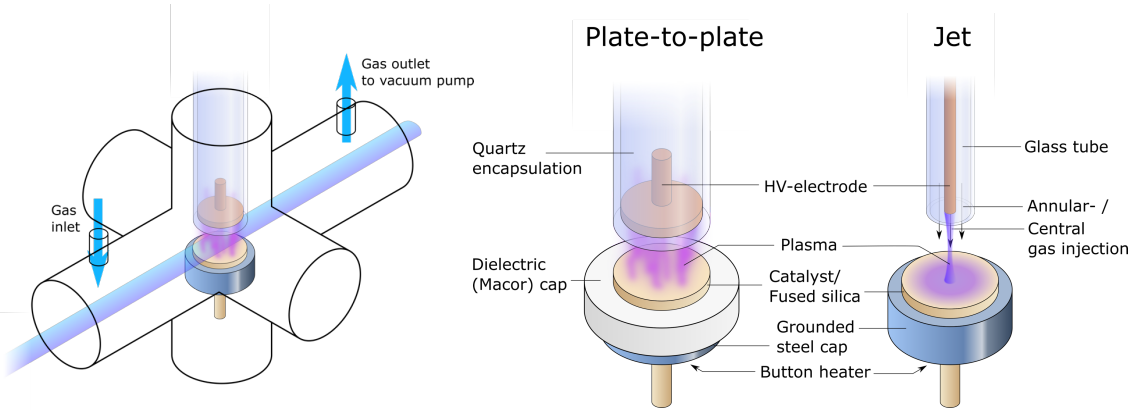

Figure 2: *(left) 6-arm quartz cell; (center & right) heater and plasma electrode geometry for plane-to-plane (center) and jet (right) configurations.*

The high-voltage and ground electrodes are mounted in the top and bottom arms of the cell, respectively. The top electrode can be configured with either a flat copper electrode or a plasma jet that impinges on the ground electrode. In the former configuration, a 20 mm OD copper high-voltage electrode is encapsulated in a 25.4 mm OD, flat-bottom fused silica tube. The gap between the high-voltage and ground electrodes is adjustable and was set to a separation of approximately 10 mm. The pulsed plasma was generated by connecting the top electrode to a high-voltage pulser (Transient Plasma Systems, SSPG-20X-100K). In the jet configuration, the top electrode is replaced by a 12.7 mm OD, 10mm ID glass tube and a concentric 6 mm OD steel high-voltage electrode. This electrode is hollow and is used to inject gas at the jet centerline. Additionally, there is a co-flow in the annulus between the electrode and glass tube.

The bottom (ground) electrode has a versatile design that facilitates quick exchange of different materials or surface structures that could be exposed to the plasma. Although the present study focuses on demonstrating 2D imaging of methyl in a plasma with an inert surface, this same apparatus could be used for studying methyl in the near-surface region of a heated catalyst to provide insights into kinetics of plasma-assisted catalysis, such as methane coupling. The electrode assembly consists of a stack of disks and caps, starting with the 25.4 mm OD button heater (HeatWave Labs, 101275-27), depicted schematically in figure 2 (center). The heater has a resistive heating element encapsulated in alumina, allowing operation up to 1200 K even in high pressure oxidative environments, although the temperatures used in the present experiments did not exceed 500 K. The heater is covered with a 30.5 mm OD steel cap that acts as a grounded electrode. A thermocouple is sandwiched between heater and steel cap to measure the approximate surface temperature. A 35.6 mm OD machinable ceramic (Macor) cap is placed on top of the steel ground electrode to act as a dielectric barrier. The Macor cap has a 1 mm high rim that is used to retain 25.4 mm OD, 3 mm thick disks of either inert or catalytic materials. A fused silica disk was used as an inert reference material in the present experiments.

For the plasma jet configuration, the Macor cap is omitted and the fused silica or catalyst disk is placed directly on the steel cap (figure 2, right). In this case, a steel cap with a 1 mm recession is used to retain the disk. This disk is the only dielectric barrier on the ground electrode, leaving a rim of exposed metal that helps to guide the plasma radially outward over the surface.

The PF-LIF diagnostic involves sequential pulsing of spatially overlapped laser sheets for photo-fragmentation and LIF-excitation, shown schematically in figure 3. The photo-fragmentation is produced by the fifth harmonic of a pulsed Nd:YAG laser (λ=212.8 nm). The LIF excitation near 390 nm is

produced by sum frequency mixing the output of a Nd:YAG-pumped tunable Rhodamine 640 dye laser at 616 nm with the residual fundamental of the Nd:YAG laser at 1064 nm. The 212.8 nm and 390 nm beams are combined on a dielectric mirror with high reflectivity at 212.8 nm and good transmission (>90%) at 390 nm. Both beams pass through a +500 mm cylindrical lens to form a laser sheet, which is focused at the center of the discharge cell.

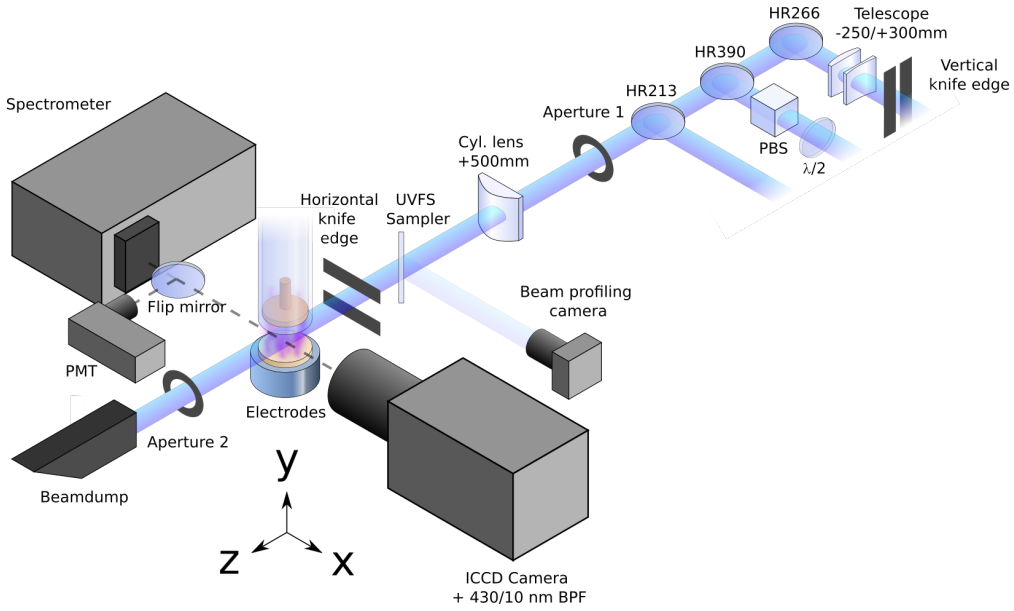

Figure 3: *Optical layout for photo-fragmentation LIF imaging (six-arm cell not shown)*

Three different fluorescence detection systems are configured on opposing arms of the quartz cell to measure the PF-LIF spectrum, temporal evolution, and 2D spatial distribution. In one arm, fluorescence is focused onto a ¼-m Czerny-Turner spectrometer, which is used to measure the fluorescence spectrum. Alternatively, by engaging a flipping mirror, the fluorescence can be steered into a photomultiplier tube (PMT) to record decay traces of the spatially averaged fluorescence. A 430 nm bandpass filter ($\Delta\lambda$=10 nm) spectrally isolates the CH fluorescence and blocks the laser wavelengths. On the opposing arm of the cell, the 2D distribution of the fluorescence signal is imaged by a gated ICCD camera (Andor iStar, DH334T 18F-63) using a similar bandpass filter. The projected pixel size for the images is 30 µm/px.

For absolute calibration, methyl is produced from photo-dissociation of acetone using a 266 nm laser sheet from the fourth harmonic of a pulsed Nd:YAG laser (10 ns pulse width, 10 Hz rep rate). The 266 nm beam is combined with the 212.8 nm and 390 nm beams by passing it through the respective steering mirrors. The 266 nm beam is formed into a 220 µm wide collimated laser sheet with a homogenous intensity profile using a combination of a cylindrical telescope and the final shared +500 mm cylindrical lens (see *absolute calibration*). Acetone vapor is introduced into the cell by flowing inert gas through a bubbler filled with liquid acetone. The inert gas is either He, N_2, or CO_2, depending on the gas mixture used in the experiments. The bubbler is connected to the gas distribution system via a needle valve, which is adjusted to regulate the pressure in the bubbler between 500-600 Torr. The pressure in the bubbler is monitored by a capacitance manometer, and the bubbler is placed in a 293K temperature-controlled water bath.

Timings of the pulser, lasers, and camera, are controlled by a set of digital delay generators. The high-voltage pulser outputs a 50 kHz, 50-pulse burst of approximately 19 kV pulses with a total duration of 1 ms, and the bursts are repeated at 10 Hz. The delay between pulsing of the 212.8 nm and 390 nm laser beams is varied between 5-30 ns to optimize the PF-LIF signal. The intensified camera gate of 100-300 ns captures the PF-LIF fluorescence and brackets the timing of the two laser pulses. During calibration, the 266 nm laser fires 1 μs before the 212.8 nm laser pulse to eliminate interference from scattering or LIF induced by the 266 nm beam. During this time, the methyl concentration does not appreciably decrease.

The three laser sheets (λ=266 nm, 212.8 nm, and 390 nm) are aligned using a combination of beam-profiler and PF-LIF measurements. A removable fused silica wedge is used for sampling the beams into a beam profiling camera. The profiling camera is positioned at the 212.8 nm beam waist, ensuring it records the same beam profile that is present in the center of the discharge cell. The 390nm sheet is slightly defocused to increase overlap with the 212.8 nm sheet and reduce the effect of beam walk-off on the signal intensity. Overlap of all the laser sheets is optimized by flowing acetone vapor through the discharge cell and aligning the laser beams to maximize the PF-LIF signal.

3. Absolute Calibration

3.1 Methyl production

Absolute calibration of the PF-LIF signal is achieved by producing a known mole fraction of methyl via photo-dissociation of acetone. The dominant pathway for acetone photo-dissociation at 266 nm produces ground-state methyl and excited-state CH_3CO fragments:

$$(CH_3)_2CO + h\nu \rightarrow CH_3 + CH_3CO^* \qquad \text{R1}$$

The CH_3CO fragment carries a large fraction of the excess energy [Lee2017]. For dissociation at higher photon energies, this can result in decomposition of the CH_3CO fragment and production of a second methyl radical [North1995]:

$$CH_3CO^* \rightarrow CH_3 + CO, \qquad \text{R2}$$

However, for excitation at 266 nm, the energy in the CH_3CO^* fragment is insufficient for the second dissociation step (R2), resulting in a single methyl radical per photo-dissociation reaction (R1). The laser-produced methyl mole fraction x_{CH_3} is then given by:

$$x_{CH_3}(\vec{r},T) = x_{ace}\eta_{exc}(\vec{r},T)Y_{CH_3}, \qquad \text{Eq 1}$$

where x_{ace} is the acetone mole fraction, η_{exc} is the fraction of acetone molecules excited by the laser, and $Y_{CH_3} = 0.93$ is the methyl yield by photo-dissociation of acetone [Khamaganov2007]. To calculate the acetone mole fraction, it is assumed that the flow through the acetone bubbler is saturated with acetone. The pressure at the exit of the bubbler is monitored, and the mole fraction is the ratio of the vapor pressure over the measured total pressure. The acetone vapor pressure is a function of temperature and is calculated through Antoine's equation using coefficients from NIST [Ambrose1974]. The value of η_{exc} is also a function of temperature, as well as position, and is given by:

$$\eta_{exc}(\vec{r},T) = \frac{F(\vec{r})\sigma(T)}{h\nu}, \qquad \text{Eq 2}$$

where $F(\vec{r})$ is the 266 nm laser fluence, $\sigma(T)$ is the absorption cross-section of acetone, and $h\nu$ is the photon energy. The temperature dependent cross-section is taken from Thurber et al., with a value of $4.4 \cdot 10^{-20}$ cm^2 at 296 K and an uncertainty of 2-3% [Thurber1998].

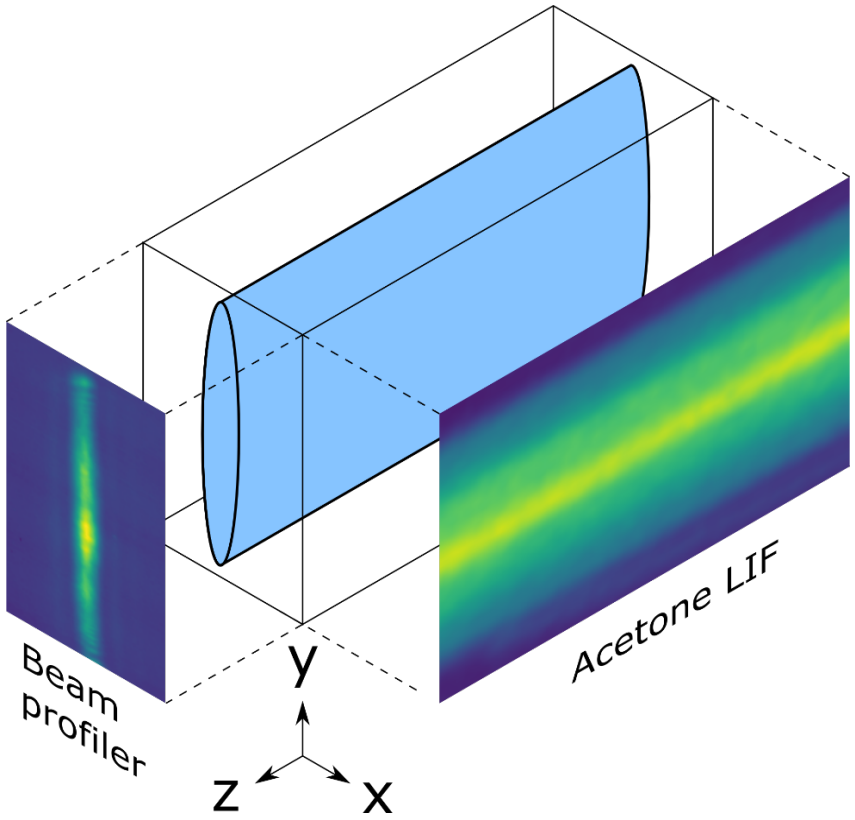

Figure 4: *Determination of laser fluence. A beam profiling camera is used to determine the normalized beam profile along the X-axis. Acetone LIF is used for determining the YZ-profile.*

To calibrate the PF-LIF signals, the methyl concentration must be determined at the positions where the combined PF-LIF beams (212.8 nm and 390 nm) overlap with the 266 nm acetone photolysis beam. This procedure involves two steps. First, the spatial variations in the fluence of the photolysis laser sheet are measured. The in-plane (Y-Z axes) and out-of-plane (X-axis) profiles of the photolysis laser sheet are determined by combining beam-profiling camera measurements and acetone LIF imaging, as depicted schematically in figure 4. For the acetone LIF imaging, the 266 nm laser sheet propagates through the cell filled with a uniform acetone distribution at room temperature, and the resulting LIF signal is detected on the ICCD camera. The combination of these measurements enables registration of the 3D beam profile on the PF-LIF imaging camera. To improve the 266 nm beam profile, a smooth rectangular part of the beam is selected by cropping the beam with a vertical knife edge. A second, horizontal knife edge (figure 3) vertically copped the beam to reduce scattering along the top and bottom surfaces of the discharge cell.

For the second step of the calibration procedure, the overlapping PF-LIF laser sheets are centered on the photolysis laser sheet, and PF-LIF signals are measured with the heater activated such that the spatial variation in temperature within the cell is identical to that used for the plasma measurements. The photolysis laser sheet was significantly wider (along the X-axis in figure 4) than the other two laser sheets such that the photolysis fluence was approximately uniform in the region of overlap. For the methyl calibration, the cell is filled with a known acetone concentration, and the calibration PF-LIF signal (S^{cal})

is recorded. The methyl mole fractions in the plasma measurements $x_{CH_3}^{plasma}$ are then determined from the ratio of the PF-LIF images in the plasma S^{plasma} and calibration S^{cal}, as given by:

$$x_{CH_3}^{plasma} = \frac{S^{plasma}}{S^{cal}} x_{CH_3}^{cal} \quad \text{Eq 3}$$

This calibration approach directly yields the methyl mole fraction because the PF-LIF signal ratio accounts for spatial variations in the total number density that result from variations in the gas temperature between the two electrodes, which are produced by the heating of the bottom electrode. The variation in total number density in the calibrations is identical to that of the plasma experiments, provided that the plasma does not significantly heat up the mixture, which is confirmed to be the case by coupled energy measurements (see section 4.1). Methyl number density profiles can be obtained by multiplying Eq. 3 by the total number density, obtained by measuring the temperature profile and applying the ideal gas law.

3.2 Temperature correction

When the heater is activated, the inhomogeneous temperature profile in the gap between the electrodes introduces a spatial dependence in the laser-produced methyl density due to the variations in the total density and the temperature dependent absorption cross-section of acetone. To account for the absorption cross-section variations, the temperature profile was determined by measuring the ratio of acetone LIF-intensities at room- and elevated temperatures respectively. Using the relationship obtained by [Thurber1998], the ratio of the acetone LIF intensities yields a direct measure of the temperature. The

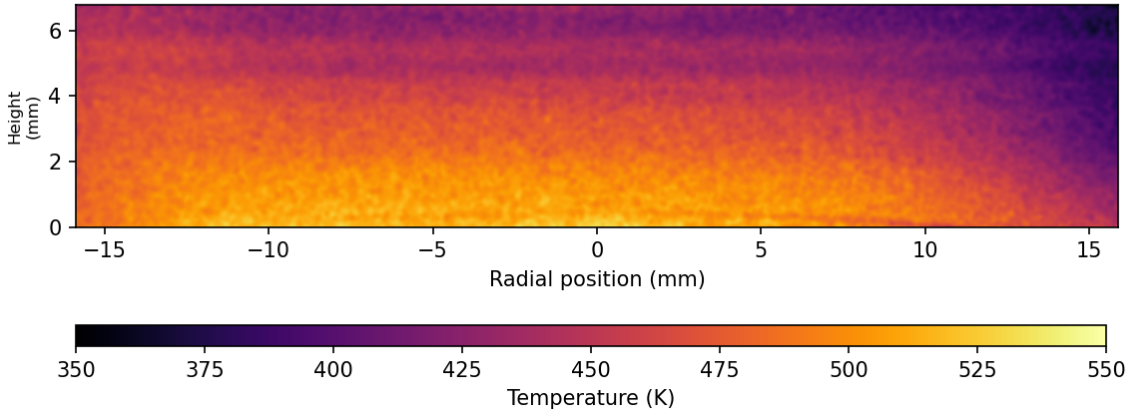

Figure 5 *Temperature profile of the gas between electrodes as determined from acetone LIF measurements.*

recorded signal was verified to be fluorescence and not phosphorescence, since addition of oxygen, which rapidly quenches phosphorescence, did not appreciably decrease the signal.

We obtain the temperature profile depicted in figure 5 for a nominal electrode temperature of 473 K. The temperature profile is uniform along most of the horizontal axis, with a gradient along the vertical axis and the highest temperatures close to the heater. The temperature measured by LIF on the hot side exceeds the temperatures of 473 K measured by the thermocouple, which may be attributed to poor

thermal contact of the thermocouple to the surface. The presence of a developing boundary layer is clearly observed on the far-right side, which is expected given that the gas flows from right to left in the figure. Some horizontal stripes are present, most visibly around a height of 5 mm, which are due to small drifts in the laser sheet profile during the period between the acquisition of the acetone LIF images at room temperature and with the heater activated. This temperature measurement is used to create a 2D spatial map of the acetone absorption cross-section, which is used in Eq. 2 to determine the fraction of acetone molecules that are dissociated at each position.

3.3 Quenching

To compare the PF-LIF intensities between calibration and experiment, we must consider the collisional quenching rates of CH LIF in these two scenarios. For most LIF schemes in which the detected fluorescence is produced by transitions directly from the laser-pumped electronic level, strategies to correct for quenching include measuring fluorescence decay rates or calculating the quenching rates by combining measurements or simulations of local species composition and temperature with knowledge of quenching rate constants [Tamura1998].

In the B-A transfer scheme used in this work, quenching is not only affected by the A-X decay rate, but also by the B-X and B-A transfer rates. In total, the quenching dynamics of this four-level system are governed by seven quenching rates per collision partner. While detailed rate constants have been obtained for some partners [Randall2000, Richmond2005], knowledge of rate constants for other molecules, notably methane, is incomplete or not available in the literature. Moreover, plasma-produced radical densities are unknown but may have a significant contribution to quenching.

We simplify the CH-LIF quenching correction by measuring LIF signals for the calibration and experiment under the same quenching conditions. In addition to using identical temperature profiles, we use a gas mixture that contains a sufficiently large fraction of a strong quencher, in this case methane, to ensure that the quenching is dominated by this species and is not significantly influenced by minor species, such as acetone that is seeded into the gas mixture during calibration or plasma-produced radicals in the experiment.

The LIF signal is most sensitive to quenching when probing in the linear regime. To further reduce sensitivity to differences in quenching, we operate in the saturated regime by using sufficiently high laser intensities to strongly saturate the B-level. To confirm that the pumping rates of the B state were well within the saturated regime, we performed an LIF energy dependence scan by varying the 390 nm pulse energy with a half-wave plate-polarizer combination while keeping the plasma power and 212.8 nm laser energy constant. Although saturated LIF schemes introduce additional complications such as variations in the extent of saturation over the spatiotemporal profile of the laser beam, these issues are of lesser importance for the current measurements because these saturation effects are incorporated into the calibration procedure.

In an LIF-scheme involving only a single excited electronic level, the saturation-LIF signal is ideally insensitive to quenching. In the B-A transfer scheme however, the saturated B-X transition only eliminates sensitivity to quenching of the B state. A complete quenching correction would also require accounting for B-A and A-X quenching rates. Quenching rates from the A-state could in principle be obtained by fitting the A-X decay traces [Richmond2005], but the partner-dependent B-A quenching rates would still be unknown when the local composition is unknown. This indicates that even when employing saturation-LIF, one must still rely on the similarity between calibration and experiment quenching environments to correctly account for quenching rates.

Measurements of the A-X fluorescence decay rate are used to determine the similarity of quenching environments between the calibration and experiment. A photo-multiplier tube was used in combination with a 430 nm bandpass filter ($\Delta\lambda$=10 nm) to record fluorescence decay traces from the overlapping A-X (0,0) and A-X(1,1) bands. As mentioned above, the decay traces cannot be used directly to correct for quenching in our B-A LIF scheme. It is assumed however, that the decay traces are a good measure for how similar the quenching environments are between calibration and experiment, and whether quenching is indeed dominated by methane.

The methane fraction in a CH_4/N_2 mixture was varied while recording the PMT traces. Methyl was produced either by a plasma discharge, or by photo-dissociation of acetone using the 266 nm laser. In both cases, 0.8% of acetone (by volume) was present and only the 212.8 nm laser was used for excitation. Since we are only interested in the A-X decay rates in this instance, we could measure the decay either from PF-LIF signals produced by the two lasers, or by measuring fluorescence from electronically excited CH(A) that is produced directly in the photo-fragmentation process (LPIF), by the 212.8 nm laser alone. Since both processes involve decay from the A-state, both LPIF and PF-LIF schemes yield the same A-X fluorescence decay traces. For the stronger quenching environments where quenching times can be on the order of a few tens of ns, the presence of 390 nm scattering and broadband fluorescence of the surfaces in the PF-LIF scheme interferes with the A-X decay traces, which complicates the retrieval of reliable decay times. For this reason, LIF excitation by the 390 nm was omitted to produce cleaner fluorescence time traces from excitation directly by the 212.8 nm laser. The issue of the 390 nm laser beam interfering with the decay traces does not arise when acquiring the PF-LIF images, because scattering from the 390 nm laser and fluorescence of the surfaces, which originates mostly from the side where the laser hits the sample holder, is spatially separated from the PF-LIF signals in the discharge gap.

The resulting traces are shown in figure 6 for a 60 Torr plasma discharge seeded with acetone for a range of methane mole fractions between 0 and 50% (left figure). Seeding acetone during the discharge increases the methyl density, improving the signal-to-noise ratio of the decay traces. The oscillations in the traces around 50 ns are likely the result of the instrumental response of the detection system. The portion of the decay traces from 10-100 ns were fit to single-exponential decay curves, and the resulting decay rates are plotted as function of the methane mole fraction in figure 6 (right figure). The decay rates

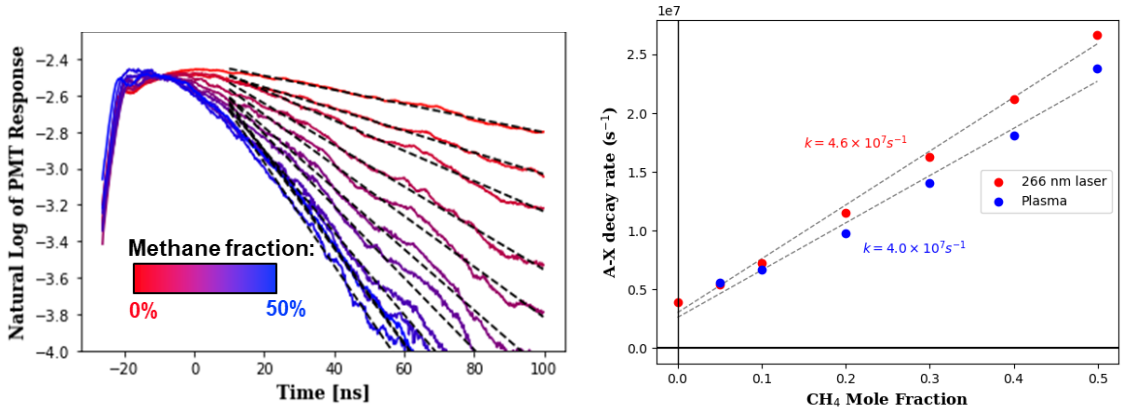

Figure 6 (left): *PMT time traces of A-X fluorescence decay for different methane mole fractions. Decay rates are obtained by fitting the traces in the region with single-exponential decays (dashed lines).* **(right)**: *CH-LIF decay rates as a function of methane mole fraction in plasma (blue dots) and in calibration measurements using photodissociation of acetone (red dots). The similarity of the decay rates indicates that quenching is comparable between the experiment and calibration.*

with and without the plasma are in decent agreement, suggesting that quenching rates are similar for the experiments and calibration. The slopes of the mole fraction dependent rates are $4.0 \cdot 10^7$ s^{-1} and $4.6 \cdot 10^7$ s^{-1} for the plasma and laser-produced methyl, respectively. The 15% discrepancy between the two rates is within the uncertainty of the measurements. The offset at 0% methane mole fraction with and without the plasma is $2.6 \cdot 10^6$ s^{-1} and $3.0 \cdot 10^6$ s^{-1}, respectively, which is attributed to quenching by the 0.8% acetone. For a mixture of 50% methane, the quenching rate is a factor of 8 larger than quenching purely by acetone, demonstrating the overwhelming contribution of methane to the total quenching rate at the conditions used in the plasma experiments.

4. Results and discussion

As a demonstration of scenarios that can be probed with the methyl diagnostic, we investigated methyl profiles in the plasma aided oxidative coupling of methane. The PF-LIF diagnostic was used to study methyl production in a nanosecond pulsed plasma in a plane-to-plane configuration to measure absolutely calibrated profiles in a diffuse discharge by flowing a methane-carbon dioxide mixture, and uncalibrated profiles in filamentary discharges by flowing a methane-oxygen mixture. The methyl profiles were compared with profiles of formaldehyde, an important intermediate in the oxidative coupling reaction. Finally, the methyl diagnostic was demonstrated in a plasma jet, where images of plasma emission, CH LIF, and CH_3 PF-LIF were obtained.

4.1 Plane-to-plane geometry

The plane-to-plane geometry produces a diffuse discharge by maintaining the cell at 200 Torr and flowing a 50/50 CO_2 and CH_4 mixture (by volume) at 2 slm. The discharge burst has a 1 ms duration and consists of 50 pulses at 19 kV and a repetition rate of 50 kHz. Current and voltage traces of the HV pulse burst are displayed in figure 7. The relative phase between the voltage and current traces was adjusted to overlap the peak of the current with the peak of the voltage time derivative. The product of current and voltage traces was integrated to obtain the coupled energy per pulse in the burst, shown for the first pulse in figure 7 in blue. The coupled energy of this first pulse was 0.66 mJ. Subsequent pulses had a higher energy, with an average value of 1.1 mJ and a standard deviation of 0.1 mJ, which corresponds to 57.4 mJ of total coupled energy for the entire pulse burst.

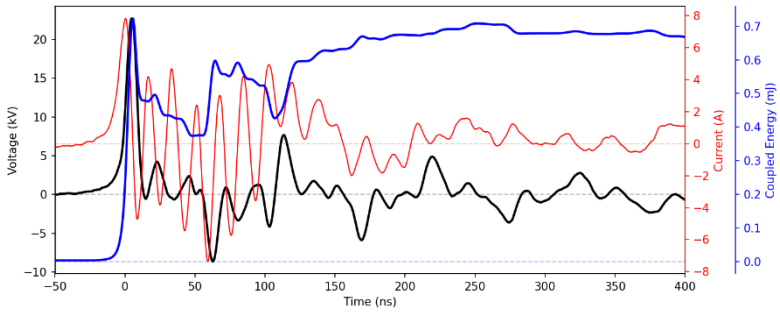

Figure 7: *Voltage, current, and coupled energy traces of the first pulse in the burst.*

An upper bound of the temperature increase due to the plasma pulse can be calculated by assuming that all this energy goes into heating of the volume. If the plasma volume is assumed to be a cylinder of 10 mm height and 25.4 mm diameter, initially at 300 K, this is equivalent to an enthalpy change of 1.1 kJ/mol. Taking into consideration the heat capacities at constant pressure for CO_2 and CH_4, this would result in a temperature increase of 29 K. Close to the surface where the initial temperature is 500 K, the coupled energy is 1.8 kJ/mol and the maximum temperature increase is 38 K.

A fused silica disk is placed on top of the Macor cap that covers the ground electrode and serves as a dielectric barrier. The fused silica disk provides an inert surface that could be replaced by a disk of catalytic material to investigate surface catalytic processes.

Single shot images of the plasma emission of individual discharge pulses, filtered by the 430 nm bandpass filter, are recorded during the pulse burst for different numbers of pulses, shown in figure 8. Although the first pulse is filamentary, all consecutive plasma pulses are diffuse and reproducible. At room temperature, methyl production was too low to achieve good signal-to-noise ratios of the PF-LIF images. However, the methyl fraction increased strongly with temperature, and a significant amount of methyl could be produced by heating the surface to 473 K. Heating the gas has the additional benefit of making the discharge more diffuse.

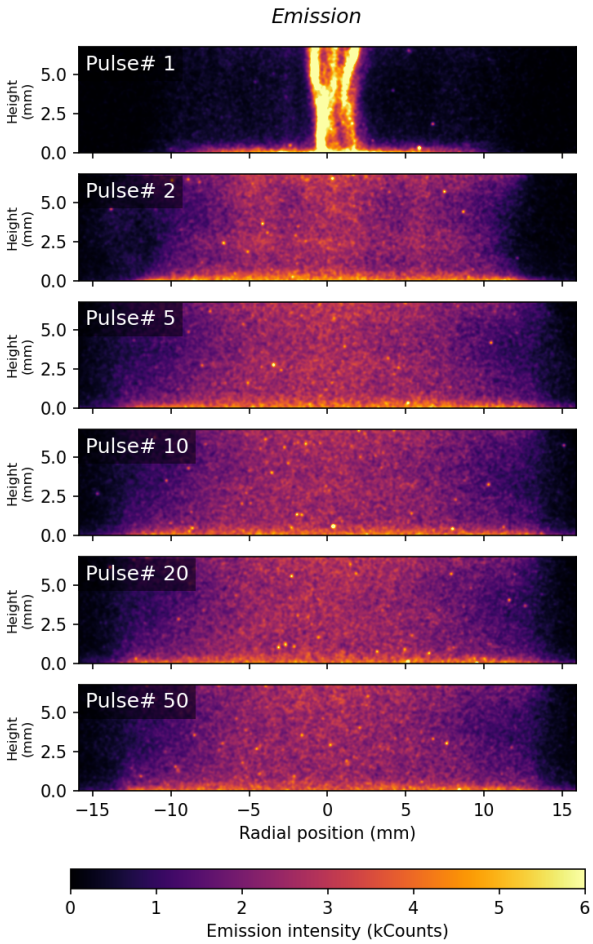

Figure 8: *Single shot emission images of individual pulses during the discharge burst*

Images of the absolute methyl mole fraction were recorded at a range of time delays during and after the discharge burst, shown in figure 9. The images are averaged over 250 shots, for a total acquisition time of 25 s per image. The profiles were corrected for plasma emission, LPIF, and CH-LIF emission, as described in more detail in appendix A1, including a discussion on their relative intensities. The bursts are repeated at 10 Hz synchronously with the lasers. The time delays Δt are given with respect to the end of the last pulse in the burst. There is some PF-LIF signal present prior to the start of each pulse burst. However, it is unlikely that this signal is the result of residual methyl from the previous pulse burst because the 99 ms interval from the end of the previous pulse is too long for the methyl to survive. Instead, the origin of this signal appears to be from a laser-induced process, such as photo-fragmentation of CH_4 by the 212.8nm beam. To correct for this background, the frame at Δt = -1 ms, which is 20 µs before the first pulse of the burst, was subtracted from all other frames. Figure 9 shows the resulting images after this subtraction.

The images taken during the pulse burst are recorded 1 µs after the stated pulse number to minimize interference from plasma emission. At pulse #1, the filamentary behavior seen in the corresponding emission image of figure 8 is clearly mirrored in the measured methyl profile. Starting at pulse #2, methyl encompasses 80-90% of the electrode width, again mirroring the emission, and the methyl profile at subsequent times remains relatively flat. Because the methyl production rate is controlled by the electron density and electric field distribution, this flat methyl profile indicates that the discharge itself is highly uniform, even on a single-shot basis. The methyl mole fraction rapidly increase in the first 5-10 shots and then increases only very slowly.

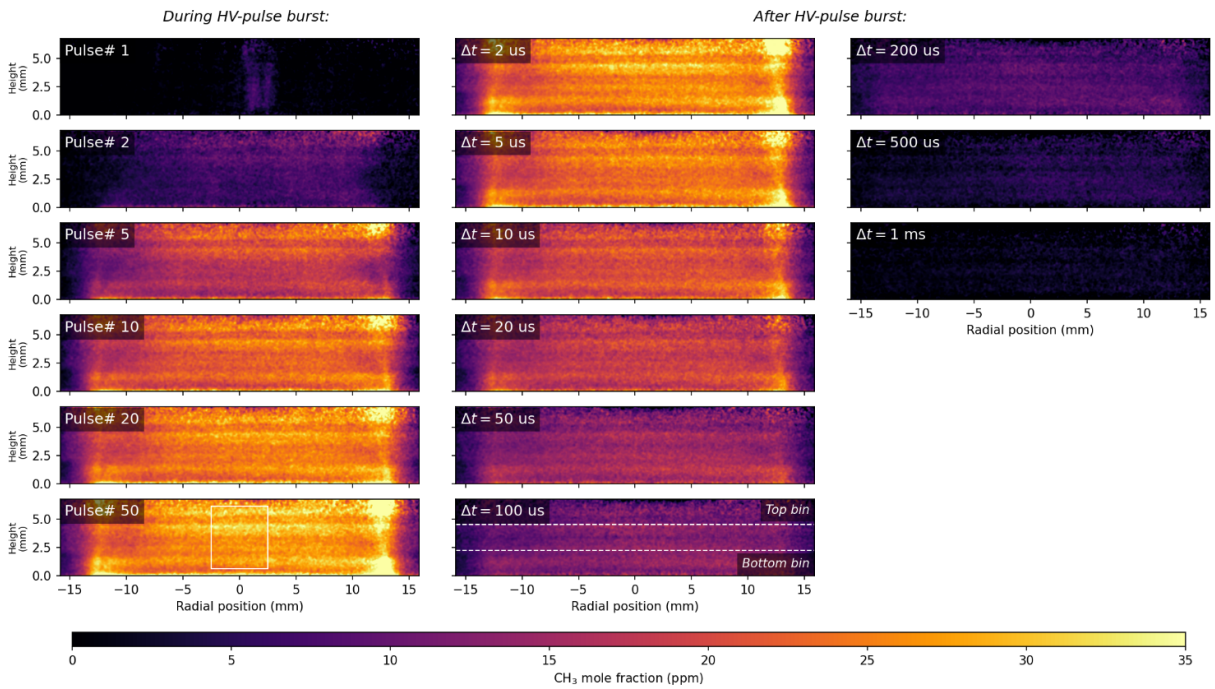

Figure 9: *Time sequence of images of methyl **mole fraction** in the plane-to-plane discharge geometry during the high-voltage pulse burst (left column) and at different time delays after the pulse burst (middle and right columns). The white rectangle in Pulse# 50 designates the area of radial binning that is used to produce the plot in Figure 10. Dashed horizontal lines in the image at Δt = 100 µs indicate the top and bottom bin used for the time evolutions in Figure 11.*

After the burst, images were acquired at increasing time intervals from 2µs to 1ms, depicted in the center and right columns of figure 9. Horizontal stripes in the mole fraction profiles are residual inhomogeneities in the laser beam profiles that were not accounted for by the beam profile corrections. In Figure 10, the vertical cross-section of the mole fraction profile of shot #50 is displayed, which is averaged over a radial distance of 5 mm around the centerline of the profile (r = 0 mm), highlighted by the white rectangle in figure 9. The inhomogeneities amount to +/- 15% of the average methyl mole fraction. Temporal fluctuations were evaluated by analyzing the data for shot #50 in five different pulse bursts. The spatially averaged standard deviation for these five resulting images was 6% of the mean mole fraction.

The overall uncertainty can be estimated by assessing the individual sources of uncertainty. The acetone absorption cross-section σ(T) has a reported uncertainty of 3% [Thurber1998]. Uncertainties in

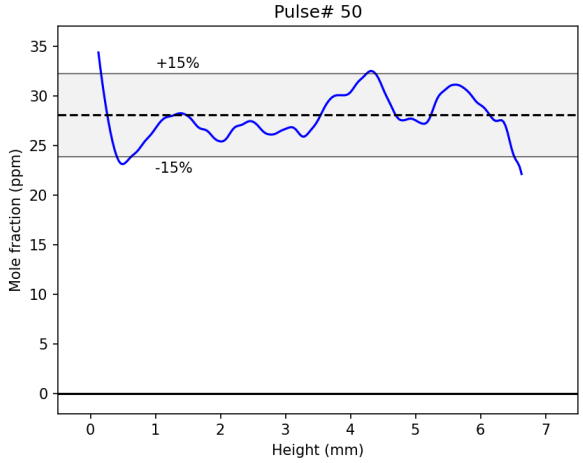

Figure 10: *Vertical cross-section of the methyl mole fraction profile as a function of height above the bottom electrode near the centerline (r = 0 mm) for shot #50. Spatial inhomogeneities due to the residual laser profile variations are within +/-15% of the mean.*

the temperature profile don't propagate significantly due to the relatively small temperature dependence (the cross-section increases by only 13% over the range of 300 K to 500 K). The acetone mole fraction x_{ace} is calculated by assuming a saturated mixture at the temperature and pressure of the bubbler. The uncertainty in the bubbler temperature and pressure results in an estimated uncertainty of 5% in x_{ace}. The methyl yield in acetone photo-dissociation Y_{CH_3} has a reported uncertainty of 10% [Khamaganov2007]. Any possible misalignment in overlap of the 213 nm and 390 nm beams does not contribute to the systematic uncertainty because the overlap is the same in the experiment and the calibration. Variations in the overlap of the 266 nm beam with the other two beams *does* contribute, because the calibration procedure presumes that the methyl is probed at the peak 266 nm laser fluence along the out-of-plane axis (X-axis). We estimate that this error should not exceed 10 %. As discussed earlier, we expect interference of CH_2 to be minimal, but we include a 10% error to account for this possible interference. Finally, a difference in collisional quenching rates between experiment and calibration adds to the overall uncertainty because the measured rates cannot be directly used to correct for spatiotemporal variations in quenching effects (see discussion in section 3.3). For the current assessment, we assume that the measured differences in A-X quenching rates are representative of the differences for all the relevant quenching rates, including the B-X rates that cannot be quantified. This would suggest the difference in quenching rates introduces an additional 15% uncertainty. Taking all these uncertainties into account by summation in quadrature, we estimate an overall uncertainty in the methyl mole fraction of 24%.

The temporal decay of the methyl mole fraction following the high-voltage pulse burst is evaluated by spatially averaging the signals in figure 9 within two separate vertical bins, depicted by dashed horizontal white lines. The decay traces of the top and bottom bins, with an average temperature of 429 K and 497 K respectively, are plotted as function of time in figure 11. To facilitate a comparison of the decay rates, the traces are normalized by the respective mole fraction at the earliest time delay of 2 µs. The measured decays are compared with chemical kinetic simulations that were performed using the Chemkin code [Kee2007] to model the temporal decay of methyl in a homogeneous mixture of gases with the GRI-Mech 3.0 chemical kinetic mechanism [SmithGRI]. The initial conditions for the simulation were set to the experimental conditions with a pressure of 200 Torr, temperatures of 429 K and 497 K, and a 50/50 CH_4/CO_2 gas mixture. The initial methyl mole fraction at each temperature was set equal to the average measurement within each bin. The measured and simulated methyl decays in figure 11 show that the decay rates are nearly the same at these two temperatures. The experiments show a rapid initial decay of the methyl that is significantly faster than the corresponding predicted decays. This underprediction of the decay rates suggests that reactions of methyl with additional plasma-produced species, such as radicals, play an important role but are not included in the Chemkin calculations.

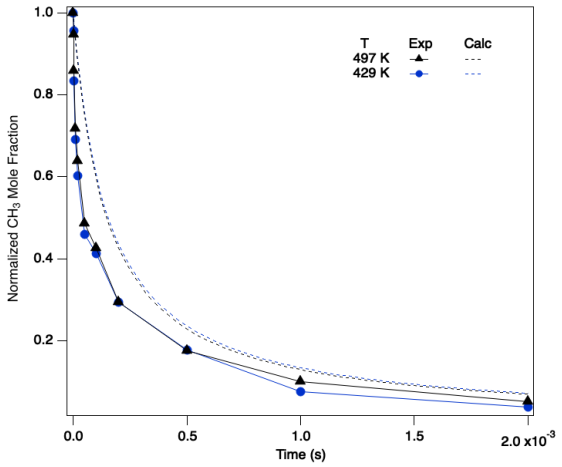

Figure 11: *Time trace of normalized methyl mole fraction in top and bottom vertical bins (see dashed lines in figure 9) with average temperatures 429K and 497K respectively. Mole fractions are normalized to the value at 2 µs delay. Dashed curves are calculated decays using Chemkin.*

4.2 Methyl & Formaldehyde

To obtain a more complete picture of plasma-enhanced methane chemistry, it is helpful to measure the temporal and spatial evolution of other intermediate species in addition to methyl. One such intermediate, formaldehyde, can be imaged by laser-induced fluorescence using the third harmonic of a Nd:YAG laser (λ=355 nm) to excite overlapping transitions in the 4_0^1 band of the $\tilde{A}^1A_2 \leftarrow \tilde{X}^1A_1$ system. Using the combination of methyl PF-LIF and formaldehyde LIF techniques, we measured the temporal and spatial evolution of both species in the plane-to-plane discharge. The same optical layout that was used for the PF-LIF was also used to record formaldehyde LIF-images, with a 355 nm excitation laser replacing the 390 nm laser. The polarization of the 355 nm beam was orthogonal to that of the 390 nm beam, which facilitated quick switching between the two laser beams using a polarizing beamsplitter cube (shown in figure 3). For detection of formaldehyde LIF, the 430 nm bandpass filter was replaced by an eleven-band bandpass filter that transmitted the formaldehyde LIF emission spectrum and blocked out-of-band interferences. The formaldehyde LIF signal was normalized by performing a separate set of measurements with the cell filled with a formaldehyde mixture that was supplied by bubbling the gas flow through a temperature-controlled bubbler containing formalin, a solution of formaldehyde, methanol, and water. Because the absolute formaldehyde concentration in the calibration mixture was not quantified, this correction yields images that are proportional to the formaldehyde mole fraction.

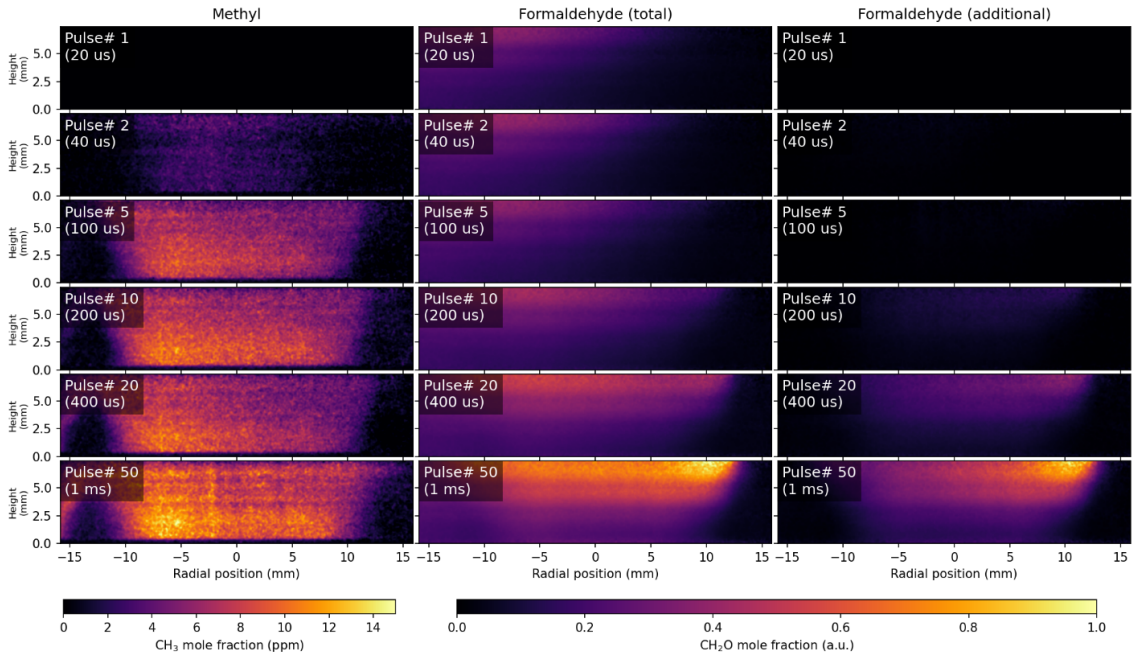

Figure 12: *Comparison of methyl mole fraction profiles and relative formaldehyde profiles (proportional to mole fraction) during the 50-pulse burst.*

We compared the temporal and spatial evolution of the production of methyl and formaldehyde in the plasma at different times during a 50-pulse high-voltage burst. For these measurements, the fused silica disk on the ground electrode was replaced by a vanadium oxide (V_2O_5) disk that was heated to 473 K. Vanadium oxide has been studied for its catalytic properties in thermal oxidative coupling reactions of hydrocarbons without a plasma [Pak1997, Doebler2005, Feyel2007], but the effects of coupling V_2O_5 with a plasma have not been established. For the demonstration of methyl and formaldehyde

measurements, the flow rate in the cell was increased by adding helium to the CO_2/CH_4 mixture (flow rates: 2 slm CO_2, 2 slm CH_4, 1 slm He), which reduced the amount of residual formaldehyde produced by the previous pulse burst. This increase in total flow compared to the results from section 4.1 results in a stronger temperature gradient, and as a result less homogeneous mole fraction profiles.

The results of the methyl/formaldehyde comparison are shown in figure 12. Methyl images were corrected for contributions from interfering processes (see appendix) and converted to mole fraction. The methyl image sequence shows the methyl mole fraction increasing rapidly during the first five pulses, followed by a slow increase up to pulse 50, as seen previously in figure 9. The initial formaldehyde distribution is concentrated in the upper left half of the images (figure 12, center column), which is the result of residual formaldehyde from the previous pulse burst being swept out by the incoming flow of fresh reactants (flow is from right to left across the image plane). The formaldehyde mole fraction can be seen to increase as the pulse burst progresses, but there is a significant delay between methyl and formaldehyde production. This is easier to appreciate after subtracting the LIF signal from the residual formaldehyde of the previous pulse burst, revealing only the newly produced formaldehyde, as shown in the right column in figure 12. While significant methyl production is observed at 100 μs, significant formaldehyde production is revealed only at 400 μs. The peak formaldehyde mole fraction is concentrated on the upper right of the images near the right edge of the electrode, corresponding to a low temperature zone that can be seen in figure 5, but is more pronounced in this case because of the higher flow rate.

The V_2O_5 surface noticeably changed color from bright orange to dull black after the plasma impinged on the heated surface for a couple of minutes. Flowing air at atmospheric pressure over the heated surface appeared to regenerate the surface to its pristine form. It is not clear whether this discoloration represented carbon deposition or reduction of the V_2O_5 to the much darker VO_2.

4.3 Methyl and formaldehyde in filamentary discharges

The methyl and formaldehyde profiles discussed in the previous section showed a relatively flat methyl profile as a result of a diffuse plasma discharge. The 2D spatially resolved measurements provided by the PF-LIF diagnostic make it ideally suited for investigation of discharges with large spatial gradients, such as filamentary discharges. It is well known that plasmas in fuel-oxygen mixtures exhibit strong filamentary behavior. We therefore demonstrate methyl and formaldehyde profiles in a filamentary methane/oxygen plasma. We used the same high-voltage pulse settings as in the diffuse plasma but

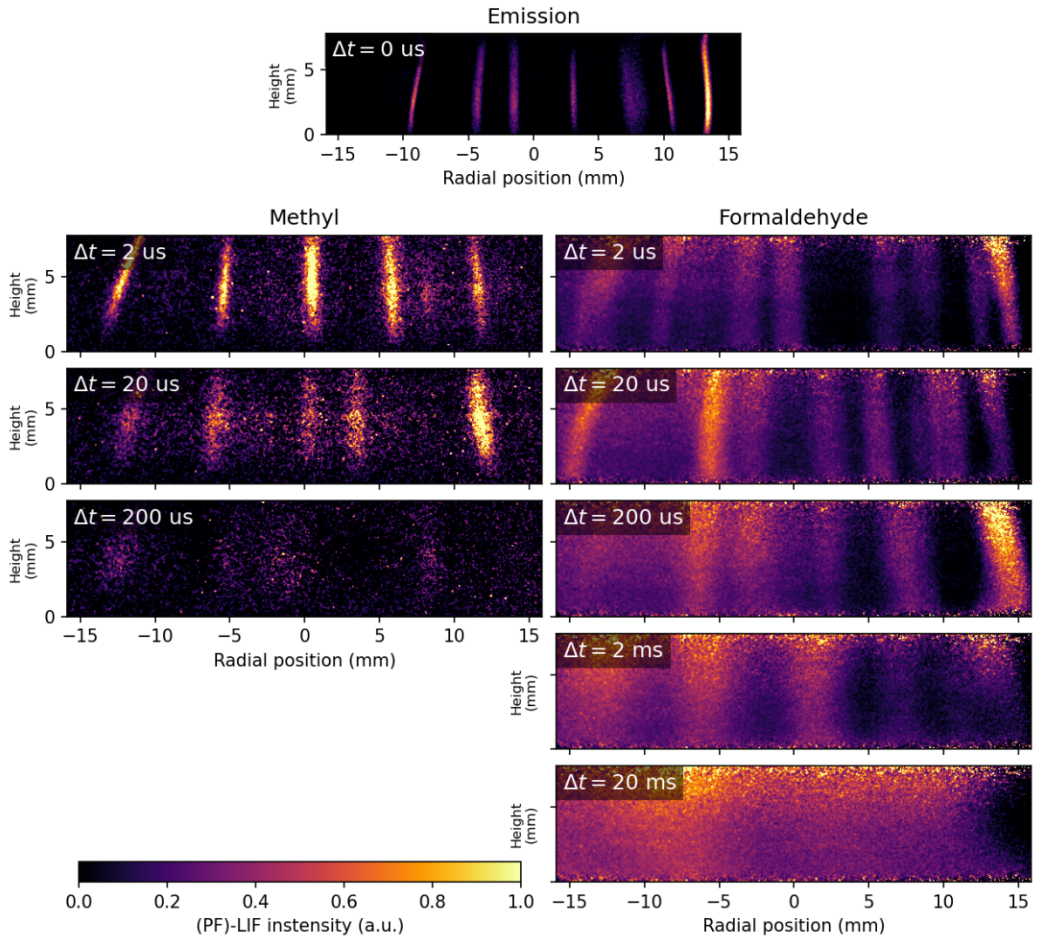

Figure 13: *Methyl and formaldehyde imaging in a filamentary plasma, 2.5 slm CH_4 + 0.5 slm O_2 at 100 Torr at different time delays after the high-voltage pulse burst. Top image shows the optical emission from the filamentary plasma during the last pulse in the burst.*

changed the gas flow and pressure to a 2.5 slm CH_4 / 0.5 slm O_2 mixture at 100 Torr without heating the surface.

The results of the recorded emission, methyl, and formaldehyde profiles are presented in figure 13. The methyl PF-LIF and formaldehyde LIF images show the evolution at different time delays following the 50-pulse plasma burst with all images acquired from separate discharge events. Due to the stochastic nature of the filaments, images that originate from different discharge events cannot be directly compared.

Nonetheless, we can observe general trends in the intensity and pattern of the filaments. Additionally, because the filaments are strongly inhomogeneous, we cannot correct for local variations in the collisional quenching environment using the approach described for the diffuse plasma. As a result, the PF-LIF and LIF images in figure 13 provide relative measurements that are corrected for variations in the laser beam profiles using the ratios of experiment and calibration images but do not provide absolute number densities.

The top image of figure 13 is a single-shot recording of emission from the last pulse in the burst (#50). It clearly displays strong filaments of approximately 1 mm in diameter. The left and right columns depict the methyl PF-LIF and formaldehyde LIF signal intensities, respectively. The (PF-)LIF signals are only produced when a filament intersects the plane of the laser sheets, whereas the emission image captures signal from filaments distributed over the entire volume of the plasma. To better compare the (PF-)LIF images with the emission images, we therefore averaged 10 frames for both the methyl PF-LIF and formaldehyde LIF.

The CH_3 PF-LIF image at 2 μs shows that the initial methyl distribution in the filaments closely resembles the optical emission of the discharge. We verified that there was no interference from plasma emission in the PF-LIF images by checking that no signal was detected with the laser beams blocked. At the longer timescale of 20 μs, the intensity of the methyl PF-LIF signal in the filaments decreases significantly. At an even longer timescale of 200 μs, the methyl density decays to substantially lower values, comparable to the signals observed for the same time delay in figure 9. At this timescale, the diameter of the methyl profiles also appears to increase as a result of the methyl diffusing outwards.

The evolution of the formaldehyde profiles tracks the emission and methyl well at the 2 μs timescale, although the diameters of the formaldehyde columns are significantly larger than those observed in the emission and methyl PF-LIF images. Unlike methyl, formaldehyde does not rapidly decay within the 20-200 μs after the discharge because it is a stable species. At longer timescales of 2-20 ms, the diameters of the formaldehyde columns increase significantly due to diffusion, forming an almost completely diffuse distribution at 20 ms. In principle, this diffuse formaldehyde could survive until the following pulse burst starts at a time delay of 99 ms. However, the lack of any significant background level of formaldehyde LIF signal at 2us after the pulse burst suggests that any residual formaldehyde from the previous pulse is destroyed in the plasma discharge before new formaldehyde is produced in the filaments.

4.4 Plasma Jet

The plasma jet provides another example of a discharge that produces strongly inhomogeneous profiles. Plasma jets are of interest for many applications that involve carbonaceous species, including CO_2 reforming of methane [Li2010], plasma assisted combustion [Kim2008], methane plasma decomposition Sanchez-Gonzalez2007], diamond film synthesis [Ohtake1990], and carbon nanotube production [Choi2006]. Imaging diagnostics in methane plasma jets have so far been limited to LIF imaging of CH [Kim2008] and OH [Iseni2014] radicals, and of tracer molecules such as acetone [Elliot2021]. In this work, we show the first application of a PF-LIF diagnostic for imaging of methyl in a methane plasma jet.

The jet configuration described in the experimental section was operated at 60 Torr with a 2 slm pure He center flow and a 1 slm CH_4 co-flow, using a nominal 12 kV discharge burst of 5 pulses at 50 kHz. The plasma jet impinges on an unheated fused silica surface, where it is guided to the grounded steel rim surrounding the disk. Figure 14(a) shows the optical emission of the jet that was detected through the 430 nm bandpass filter and recorded 10 μs after the last high-voltage pulse. The emission profile is confined to the central region of the jet where helium is injected through the hole in the high-voltage electrode.

An advantage of the PF-LIF diagnostic technique is that the distribution of the native CH radicals produced in the plasma can be readily obtained by acquiring CH-LIF images while the photo-fragmentation laser is blocked. Figure 14(b) displays the CH-LIF profile in the plasma jet, which is the difference of the images acquired with and without the 390 nm laser excitation. Note that this CH-LIF image was not corrected for the 390 nm laser profile. As a result, the distribution of CH is likely underestimated at the top and bottom of the image where the laser sheet intensity is lower.

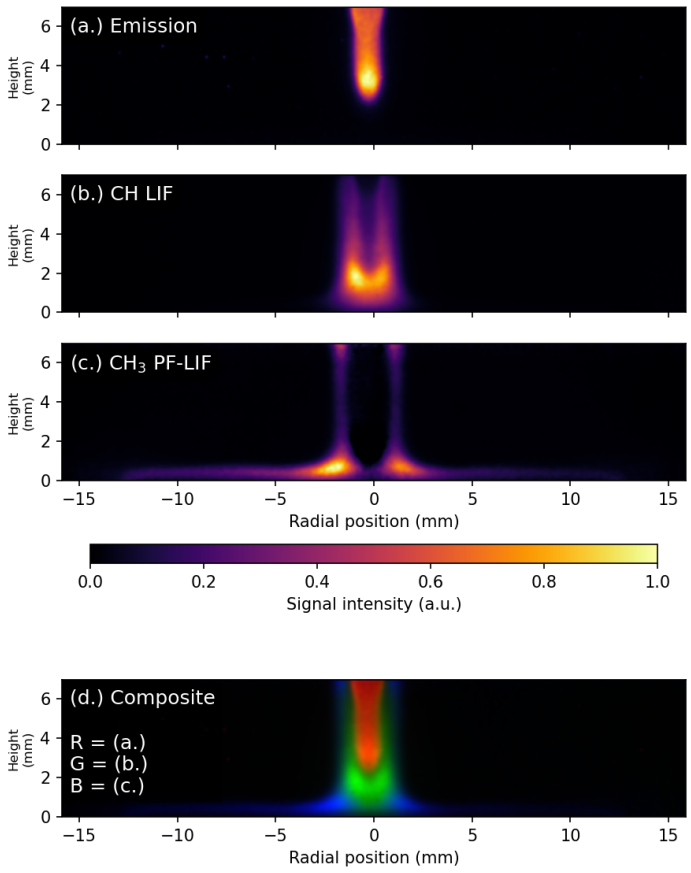

Figure 14: *Images of plasma emission, CH LIF, and CH_3 PF-LIF in a CH_4/He plasma jet*

Figure 14(c) displays the methyl PF-LIF image which is corrected for laser-beam profiles and normalized by an acetone seeded PF-LIF calibration image, but due to aforementioned issues with quenching rate corrections cannot be interpreted on an absolute scale. The images in figures 14a-c are normalized by their respective maximum values. To better appreciate the relative locations of the signals from emission, CH, and CH_3, we combined these three images into a single composite image by using each of the images as one of the color channels of figure 14(d), with Red = emission, Green = CH LIF, Blue = CH_3 PF-LIF. The figure shows a clear progression of plasma in the pure helium core, CH produced in the mixing layer of the methane and helium, and methyl being formed at the edge closest to the methane and the dielectric surface. Methyl is also produced along the entire surface (figure 14(c)), which is beneficial for future studies of methyl surface reactions.

Due to the two separate flows of He and CH_4, the composition has significant spatial variations near the mixing interface of the central jet and co-flow. This variation results in a position-dependent fluorescence yield, which complicates the interpretation of PF-LIF signals using the presented calibration scheme. In principle, the varying yield could be accounted for by seeding both flows with the same mole fraction of acetone during the calibration procedure, which would nominally result in the same methyl density being produced by photo-dissociation everywhere in the flow such that variations in yield would be reflected by differences in fluorescence intensity. This procedure would be valid if the plasma didn't significantly alter the local quenching environment. However, unlike the plane-to-plane experiments, the plasma jet is not entirely dominated by methane quenching and thus could be quite sensitive to quenching variations due to plasma-produced radicals, particularly near the jet centerline where the flow is almost pure He. For this reason, the PF-LIF measurements in the plasma jet are only corrected for laser beam profile variations and are not calibrated with quenching corrections. Nevertheless, these results can give useful information on the distribution of CH and CH_3 radicals.

5. Conclusions

We have demonstrated the feasibility of photo-fragmentation laser induced fluorescence for 2D imaging of absolute methyl densities in a nanosecond pulse plasma in the plane-to-plane configuration. In addition, we showed experiments that demonstrate the applicability of qualitative imaging in a filamentary discharge and in a plasma jet. By directly comparing the methyl images with that of other intermediates such as formaldehyde, deeper insights into the governing kinetics can be obtained. By employing a non-resonant detection scheme based on excitation to the B state and EET to the A state of CH, profiles could be recorded within approximately 100 μm of the surface. Our electrode configuration allows for ample optical access while maintaining direct contact of the plasma to a heated inert or catalytic surface.

This work describes for the first time a procedure for absolute calibration of a PF-LIF diagnostic for methyl detection. Methyl was produced in-situ through photo-dissociation of acetone by a third overlapping laser sheet. Temperature profiles for the calibration were obtained by recording acetone LIF and taking the ratio of signals at room- and elevated temperature. The calibration procedure relies on the ability to replicate the experimental conditions in a calibration measurement where the plasma is absent. This procedure is suitable for cases in which the plasma does not significantly perturb the conditions by either removing the dominant quencher or by significantly heating up the gas. This calibration scheme is compatible with the conditions of the diffuse plane-to-plane plasma, but other calibration approaches are possible. Furthermore, by choosing a different combination of excited and detected transitions of the CH-LIF it could be possible to actively correct for quenching, eliminating the need to rely on the similarity between calibration and experiment. For example, excitation in the B-X(1,0) band and detection in the overlapping B-X(1,1) and B-X(0,0) bands is a possibility [Dilecce2010-2]. It would offer a non-resonant scheme with an off-diagonal component that still has decent intensity. Because this scheme doesn't involve EET to the A-state, it affords the possibility of using direct measurements of the LIF decay times to determine the fluorescence yield at every pixel and correct for spatial variations in quenching rates. Moreover, saturation of the LIF transition would minimize the sensitivity of the fluorescence intensity to variations in quenching rates resulting from changes in the composition or temperature.

Acknowledgements

The support of US Department of Energy Collaborative Research Center for Studies of Plasma-Assisted Combustion and Plasma Catalysis is gratefully acknowledged. This material is based upon work supported by the U.S. Department of Energy, Office of Science, Office of Fusion Energy Sciences. This research used resources of the Low Temperature Plasma Research Facility at Sandia National Laboratories, which is a collaborative research facility supported by the U.S. Department of Energy, Office of Science, Office of Fusion Energy Sciences. This article has been authored by an employee of National Technology & Engineering Solutions of Sandia, LLC under Contract No. DE-NA0003525 with the U.S. Department of Energy (DOE). The employee owns all right, title and interest in and to the article and is solely responsible for its contents. The United States Government retains and the publisher, by accepting the article for publication, acknowledges that the United States Government retains a non-exclusive, paid-up, irrevocable, world-wide license to publish or reproduce the published form of this article or allow others to do so, for United States Government purposes. The DOE will provide public access to these results of federally sponsored research in accordance with the DOE Public Access Plan https://www.energy.gov/downloads/doe-publicaccess-plan.

References

[Whitehead2016] Whitehead, J. Christopher. "Plasma–Catalysis: The Known Knowns, the Known Unknowns and the Unknown Unknowns." *Journal of Physics D: Applied Physics* 49, no. 24 (May 2016): 243001. https://doi.org/10.1088/0022-3727/49/24/243001.

[Adamovich2017] Adamovich, I, S D Baalrud, A Bogaerts, P J Bruggeman, M Cappelli, V Colombo, U Czarnetzki, et al. "The 2017 Plasma Roadmap: Low Temperature Plasma Science and Technology." *Journal of Physics D: Applied Physics* 50, no. 32 (August 16, 2017): 323001. https://doi.org/10.1088/1361-6463/aa76f5.

[Bogaerts2020] Bogaerts, Annemie, Xin Tu, J Christopher Whitehead, Gabriele Centi, Leon Lefferts, Olivier Guaitella, Federico Azzolina-Jury, et al. "The 2020 Plasma Catalysis Roadmap." *Journal of Physics D: Applied Physics* 53, no. 44 (October 28, 2020): 443001. https://doi.org/10.1088/1361-6463/ab9048.

[Ju2015] Ju, Yiguang, and Wenting Sun. "Plasma Assisted Combustion: Dynamics and Chemistry." *Progress in Energy and Combustion Science* 48 (June 1, 2015): 21–83. https://doi.org/10.1016/j.pecs.2014.12.002.

[Li2021] Li, Shangkun, Rizwan Ahmed, Yanhui Yi, and Annemie Bogaerts. "Methane to Methanol through Heterogeneous Catalysis and Plasma Catalysis." *Catalysts* 11, no. 5 (May 2021): 590. https://doi.org/10.3390/catal11050590.

[Goodwin2018] Goodwin, David G., and James E. Butler. "Theory of diamond chemical vapor deposition." Handbook of industrial diamonds and diamond films. CRC Press, 2018. 527-581.

[Minea2018] Minea, Teofil, Dirk C. M. van den Bekerom, Floran J. J. Peeters, Erwin Zoethout, Martijn F. Graswinckel, Mauritius C. M. van de Sanden, Toine Cents, Leon Lefferts, and Gerard J. van Rooij. "Non-Oxidative Methane Coupling to C2 Hydrocarbons in a Microwave Plasma Reactor." *Plasma Processes and Polymers* 15, no. 11 (2018): 1800087. https://doi.org/10.1002/ppap.201800087.

[Pei2010] Pei, Qing-Xiang, Yong-Wei Zhang, and Vivek B Shenoy. "Mechanical Properties of Methyl Functionalized Graphene: A Molecular Dynamics Study," 2010, 9.

[Somers2012] Somers, W., A. Bogaerts, A. C. T. van Duin, and E. C. Neyts. "Plasma Species Interacting with Nickel Surfaces: Toward an Atomic Scale Understanding of Plasma-Catalysis." *The Journal of Physical Chemistry C* 116, no. 39 (October 4, 2012): 20958–65. https://doi.org/10.1021/jp307380w.

[Neyts2016] Neyts, Erik C. "Plasma-Surface Interactions in Plasma Catalysis." *Plasma Chemistry and Plasma Processing* 36, no. 1 (January 1, 2016): 185–212. https://doi.org/10.1007/s11090-015-9662-5.

[Chawdhury2021] Chawdhury, Piu. "A Promising Plasma-Catalytic Approach towards Single-Step Methane Conversion to Oxygenates at Room Temperature," 2021, 13.

[Scherer1997] Scherer, J. J., Aniolek, K. W., Cernansky, N. P., & Rakestraw, D. J. (1997). Determination of methyl radical concentrations in a methane/air flame by infrared cavity ringdown laser absorption spectroscopy. The Journal of chemical physics, 107(16), 6196-6203.

[Meier1987] Meier, U., & Kohse-Höinghaus, K. (1987). REMPI detection of CH3 in low-pressure flames. Chemical physics letters, 142(6), 498-502.

[Wu2011] Wu, Y., Bottom, A., Zhang, Z., Ombrello, T. M., & Katta, V. R. (2011). Direct measurement of methyl radicals in a methane/air flame at atmospheric pressure by radar REMPI. Optics express, 19(24), 23997-24004.

[McIlroy2000] McIlroy, A., Hain, T. D., Michelsen, H. A., & Cool, T. A. (2000). A laser and molecular beam mass spectrometer study of low-pressure dimethyl ether flames. Proceedings of the Combustion Institute, 28(2), 1647-1653.

[Taatjes2008] Taatjes, C. A., Osborn, D. L., Selby, T. M., Meloni, G., Fan, H., & Pratt, S. T. (2008). Absolute photoionization cross-section of the methyl radical. The Journal of Physical Chemistry A, 112(39), 9336-9343.

[Zhou2021] B. Zhou, E. Huang, R. Almeida, S. Gurses, A. Ungar, J. Zetterberg, A. Kulkarni, C.X. Kronawitter, D.L. Osborn, N. Hansen, J.H. Frank, Near-Surface Imaging of the Multicomponent Gas Phase above a Silver Catalyst during Partial Oxidation of Methanol, ACS Catalysis 11 (2021) 155-168.

[Sick1995] Sick, V., Bui-Pham, M. N., & Farrow, R. L. (1995). Detection of methyl radicals in a flat flame by degenerate four-wave mixing. Optics letters, 20(19), 2036-2038.

[Hanson1988] R.K. Hanson, Combustion diagnostics: Planar imaging techniques, Proc. Combust. Inst. 21 (1988) 1677-1691.

[Kaminski2002] C. F. Kaminski and M. B. Long, in Applied Combustion Diagnostics, edited by K. Kohse-Hoinghaus and J. B. Jeffries (Taylor and Francis, New York, 2002).

[Kohse-Hoinghaus2005] K. Kohse-Hoinghaus, R.S. Barlow, M. Alden, J. Wolfrum, Combustion at the focus: laser diagnostics and control, Proc. Combust. Inst. 30 (2005) 89-123.

[Sainct2014] Sainct, F. P., D. A. Lacoste, M. J. Kirkpatrick, E. Odic, and C. O. Laux. "Temporal Evolution of Temperature and OH Density Produced by Nanosecond Repetitively Pulsed Discharges in Water Vapour at Atmospheric Pressure." *Journal of Physics D: Applied Physics* 47, no. 7 (January 2014): 075204. https://doi.org/10.1088/0022-3727/47/7/075204.

[Schmidt2014] Schmidt, J. B., N. Jiang, and B. N. Ganguly. "Nitric Oxide PLIF Measurement in a Point-to-Plane Pulsed Discharge in Vitiated Air of a Propane/Air Flame." *Plasma Sources Science and Technology* 23, no. 6 (August 2014): 065005. https://doi.org/10.1088/0963-0252/23/6/065005.

[Ouaras2018] Ouaras, K., L. Magne, S. Pasquiers, P. Tardiveau, P. Jeanney, and B. Bournonville. "OH Density Measured by PLIF in a Nanosecond Atmospheric Pressure Diffuse Discharge in Humid Air under Steep High Voltage Pulses." *Plasma Sources Science and Technology* 27, no. 4 (April 2018): 045002. https://doi.org/10.1088/1361-6595/aab4b7.

[Frank2021] J.H. Frank, Advances in imaging of chemically reacting flows, The Journal of Chemical Physics 154 (2021) 040901.

[vandenBekerom2021] Bekerom, D C M van den, E R Jans, and I V Adamovich. "NO PLIF Flow Visualization and Time-Resolved Temperature Distributions in Laser Induced Breakdown Plumes." Journal of Physics D: Applied Physics 54, no. 26 (July 1, 2021): 265201. https://doi.org/10.1088/1361-6463/abf36f.

[Lee2017] Lee, Kin Long Kelvin, Klaas Nauta, and Scott H Kable. "Photodissociation of Acetone from 266 to 312 Nm: Dynamics of CH3 + CH3CO Channels on the S0 and T1 States." J. Chem. Phys., 2017, 13.

[North1995] North, S. W., Blank, D. A., Gezelter, J. D., Longfellow, C. A., & Lee, Y. T. (1995). Evidence for stepwise dissociation dynamics in acetone at 248 and 193 nm. The Journal of chemical physics, 102(11), 4447-4460.

[Khamaganov2007] Khamaganov, V, R Karunanandan, A Rodriguez, and J N Crowley. “Photolysis of CH3C(O)CH3 (248 Nm, 266 Nm), CH3C(O)C2H5 (248 Nm) and CH3C(O)Br (248 Nm): Pressure Dependent Quantum Yields of CH3 Formation,” 2007, 17.

[Ambrose1974] Ambrose, D., C. H. S. Sprake, and R. Townsend. “Thermodynamic Properties of Organic Oxygen Compounds XXXIII. The Vapour Pressure of Acetone.” *The Journal of Chemical Thermodynamics* 6, no. 7 (July 1, 1974): 693–700. https://doi.org/10.1016/0021-9614(74)90119-0.

[Tamura1998] Tamura, Masayuki, Pamela A. Berg, Joel E. Harrington, Jorge Luque, Jay B. Jeffries, Gregory P. Smith, and David R. Crosley. “Collisional Quenching of CH(A), OH(A), and NO(A) in Low Pressure Hydrocarbon Flames.” *Combustion and Flame* 114, no. 3–4 (August 1998): 502–14. https://doi.org/10.1016/S0010-2180(97)00324-6.

[Thurber1998] Thurber, Mark C., Frédéric Grisch, Brian J. Kirby, Martin Votsmeier, and Ronald K. Hanson. “Measurements and Modeling of Acetone Laser-Induced Fluorescence with Implications for Temperature-Imaging Diagnostics.” *Applied Optics* 37, no. 21 (July 20, 1998): 4963. https://doi.org/10.1364/AO.37.004963.

[Desgroux1996] Desgroux, P., L. Gasnot, B. Crunelle, and J.F. Pauwels. “CH3 Detection in Flames Using Photodissociation-Induced Fluorescence.” *Symposium (International) on Combustion* 26, no. 1 (January 1996): 967–74. https://doi.org/10.1016/S0082-0784(96)80309-2.

[Li2015] Li, Bo, Xiaofeng Li, Mingfa Yao, and Zhongshan Li. “Methyl Radical Imaging in Methane–Air Flames Using Laser Photofragmentation-Induced Fluorescence.” *Applied Spectroscopy* 69, no. 10 (October 1, 2015): 1152–56. https://doi.org/10.1366/15-07869.

[Li2017] Li, Bo, Dayuan Zhang, Mingfa Yao, and Zhongshan Li. “Strategy for Single-Shot CH3 Imaging in Premixed Methane/Air Flames Using Photofragmentation Laser-Induced Fluorescence.” *Proceedings of the Combustion Institute* 36, no. 3 (January 1, 2017): 4487–95. https://doi.org/10.1016/j.proci.2016.07.082.

[Wan2021] Wan, Minggang, Mingbo Sun, Ge Wu, Qiang Gao, Bo Li, Hongbo Wang, Yongchao Sun, and Jiajian Zhu. “Quantitative Feature Extraction of Turbulent Premixed Flames by Photofragmentation Laser-Induced Fluorescence.” *Optical Engineering* 60, no. 2 (February 2021): 023108. https://doi.org/10.1117/1.OE.60.2.023108.

[Wan2022] Wan, Minggang, Mingbo Sun, Ge Wu, Qiang Gao, Bo Li, Hongbo Wang, Yongchao Sun, and Jiajian Zhu. “Simultaneous CH3 and CH2O Imaging in Premixed Turbulent Flames for Instantaneous Flame Structure Visualization.” Acta Astronautica, 2022, 9. https://doi.org/10.1016/j.actaastro.2021.10.026.

[Gardiner1987] Gardiner, W. C., S. M. Hwang, and M. J. Rabinowitz. “Shock Tube and Modeling Study of Methyl Radical in Methane Oxidation.” Energy & Fuels 1, no. 6 (November 1987): 545–49. https://doi.org/10.1021/ef00006a016.

[Wang2017] Wang, Shengkai, David F. Davidson, Jay B. Jeffries, and Ronald K. Hanson. “Time-Resolved Sub-Ppm CH3 Detection in a Shock Tube Using Cavity-Enhanced Absorption Spectroscopy with a Ps-Pulsed UV Laser.” *Proceedings of the Combustion Institute* 36, no. 3 (January 1, 2017): 4549–56. https://doi.org/10.1016/j.proci.2016.08.012.

[Scarduelli2011] Scarduelli, Giorgina, Graziano Guella, Daniela Ascenzi, and Paolo Tosi. “Synthesis of Liquid Organic Compounds from CH4 and CO2 in a Dielectric Barrier Discharge Operating at Atmospheric Pressure.” *Plasma Process. Polym.*, 2011, 7.

[Deesgroux1996] Desgroux, P., L. Gasnot, B. Crunelle, and J.F. Pauwels. “CH3 Detection in Flames Using Photodissociation-Induced Fluorescence.” *Symposium (International) on Combustion* 26, no. 1 (January 1996): 967–74. https://doi.org/10.1016/S0082-0784(96)80309-2.

[Li2015] Li, Bo, Xiaofeng Li, Mingfa Yao, and Zhongshan Li. “Methyl Radical Imaging in Methane–Air Flames Using Laser Photofragmentation-Induced Fluorescence.” *Applied Spectroscopy* 69, no. 10 (October 1, 2015): 1152–56. https://doi.org/10.1366/15-07869.

[Li2017] Li, Bo, Dayuan Zhang, Mingfa Yao, and Zhongshan Li. “Strategy for Single-Shot CH3 Imaging in Premixed Methane/Air Flames Using Photofragmentation Laser-Induced Fluorescence.” *Proceedings of the Combustion Institute* 36, no. 3 (January 1, 2017): 4487–95. https://doi.org/10.1016/j.proci.2016.07.082.

[Wan2021] Wan, Minggang, Mingbo Sun, Ge Wu, Qiang Gao, Bo Li, Hongbo Wang, Yongchao Sun, and Jiajian Zhu. “Quantitative Feature Extraction of Turbulent Premixed Flames by Photofragmentation Laser-Induced Fluorescence.” *Optical Engineering* 60, no. 2 (February 2021): 023108. https://doi.org/10.1117/1.OE.60.2.023108.

[Jacob1994] Jacob, W, M Engelhard, W Möller, and A Koch. “Absolute Density Determination of CH Radicals in a Methane Plasma,” 1994, 4.

[Dilecce2010-1] Dilecce, G., P. F. Ambrico, and S. De Benedictis. “CH Spectroscopic Observables in He–CH4and N2–CH4atmospheric Pressure Dielectric Barrier Discharges.” *Journal of Physics D: Applied Physics* 43, no. 12 (March 2010): 124004. https://doi.org/10.1088/0022-3727/43/12/124004.

[Dilecce2010-2] Dilecce, G, P F Ambrico, M Simek, and S De Benedictis. “LIF Diagnostics in Volume and Surface Dielectric Barrier Discharges at Atmospheric Pressure.” *Journal of Physics*, 2010, 7.

[Tsujishita1993] Tsujishita, Masahide, Masamichi Ipponmatsu Masamichi Ipponmatsu, and Akira Hirano Akira Hirano. “Visualization of the CH Molecule by Exciting C2Σ+(V=1) State in Turbulent Flames by Planar Laser-Induced Fluorescence.” *Japanese Journal of Applied Physics* 32, no. 12R (December 1, 1993): 5564. https://doi.org/10.1143/JJAP.32.5564.

[Li2007] Li, Z. S., J. Kiefer, J. Zetterberg, M. Linvin, A. Leipertz, X. S. Bai, and M. Aldén. “Development of Improved PLIF CH Detection Using an Alexandrite Laser for Single-Shot Investigation of Turbulent and Lean Flames.” *Proceedings of the Combustion Institute* 31, no. 1 (January 1, 2007): 727–35. https://doi.org/10.1016/j.proci.2006.08.015.

[Carter2014] Carter, Campbell D., Stephen Hammack, and Tonghun Lee. “High-Speed Planar Laser-Induced Fluorescence of the CH Radical Using the $$C^{ 2} \varSigma ^{ + } {-}X^{ 2} \varPi \left({0,0} \right)$$band.” *Applied Physics B* 116, no. 3 (September 1, 2014): 515–19. https://doi.org/10.1007/s00340-014-5899-6.

[Paul1994] Paul, P. H., and J. E. Dec. “Imaging of Reaction Zones in Hydrocarbon–Air Flames by Use of Planar Laser-Induced Fluorescence of CH.” Optics Letters 19, no. 13 (July 1, 1994): 998–1000. https://doi.org/10.1364/OL.19.000998.

[Kiefer2008] Kiefer, J., Z.S. Li, J. Zetterberg, X.S. Bai, and M. Aldén. "Investigation of Local Flame Structures and Statistics in Partially Premixed Turbulent Jet Flames Using Simultaneous Single-Shot CH and OH Planar Laser-Induced Fluorescence Imaging." Combustion and Flame 154, no. 4 (September 2008): 802–18. https://doi.org/10.1016/j.combustflame.2008.04.002.

[Bergthorson2005] J.M. Bergthorson, D.G. Goodwin, P.E. Dimotakis, Proc. Combust. Inst. 30 (2005) 1637.

[Tanahashi2005] M. Tanahashi, S.Murakami,G.-M.Choi,Y.Fukuchi, T.Miyauchi, Proc. Combust. Inst. 30 (2005) 1665.

[Carter1998] C.D. Carter, J.M. Donber, J.F. Driscoll, Appl. Phys. B 66 (1998) 129.

[Vagelopoulos2005] C.M. Vagelopoulos, J.H. Frank, Proc. Combust. Inst. 30 (2005) 241.

[Watson2002] K.A. Watson, K.M. Lyons, C.D. Carter, J.M. Donbar, Proc. Combust. Inst. 29 (2002) 1905.

[Hammack2017] Hammack, Stephen D. "CH PLIF and PIV Implementation Using C-X (0,0) and Intra-Vibrational Band Filtered Detection," 2017, 5.

[Luque1996-1] Luque, Jorge, Gregory Smith, and David Crossley. "Quantitative CH Determinations in Low-Pressure Flames." *Symposium (International) on Combustion* 26, no. 1 (January 1, 1996): 959–66. https://doi.org/10.1016/S0082-0784(96)80308-0.

[Luque1996-2] Luque, J., and D. R. Crosley. "Absolute CH Concentrations in Low-Pressure Flames Measured with Laser-Induced Fluorescence." *Applied Physics B* 63, no. 1 (July 1, 1996): 91–98. https://doi.org/10.1007/BF01112843.

[Luque1997] Luque, J, W Juchmann, and J B Jeffries. "Absolute Concentration Measurements of CH Radicals in a Diamond-Depositing Dc-Arcjet Reactor." *Applied Optics* 36, no. 15 (May 20, 1997): 10.

[Luque2002] Luque, J., R.J.H. Klein-Douwel, J.B. Jeffries, G.P. Smith, and D.R. Crosley. "Quantitative Laser-Induced Fluorescence of CH in Atmospheric Pressure Flames." *Applied Physics B* 75, no. 6 (November 1, 2002): 779–90. https://doi.org/10.1007/s00340-002-1038-x.

[Juckmann1998] Juchmann, W., H. Latzel, D. I. Shin, G. Peiter, T. Dreier, H. -R. Volpp, J. Wolfrum, R. P. Lindstedt, and K. M. Leung. "Absolute Radical Concentration Measurements and Modeling of Low-Pressure CH4/O2/NO Flames." *Symposium (International) on Combustion*, Twenty-Seventh Sysposium (International) on Combustion Volume One, 27, no. 1 (January 1, 1998): 469–76. https://doi.org/10.1016/S0082-0784(98)80436-0.

[Bohm2005] Bohm. "Absolute Radical Concentration Measurements in Low-Pressure H2/O2 Flames during the Combustion of Graphite | Elsevier Enhanced Reader," 2005. https://doi.org/10.1016/j.proci.2004.08.002.

[Walsh1998] Walsh, K.T., M.B. Long, M.A. Tanoff, and M.D. Smooke. "Experimental and Computational Study of CH, CH*, and OH* in an Axisymmetric Laminar Diffusion Flame." *Symposium (International) on Combustion* 27, no. 1 (January 1998): 615–23. https://doi.org/10.1016/S0082-0784(98)80453-0.

[Gibaud2005] Gibaud, Christophe, Jordan A. Snyder, Volker Sick, and R. Peter Lindstedt. "Laser-Induced Fluorescence Measurements and Modeling of Absolute CH Concentrations in Strained Laminar Methane/Air Diffusion Flames." *Proceedings of the Combustion Institute* 30, no. 1 (January 1, 2005): 455–63. https://doi.org/10.1016/j.proci.2004.08.006.

[Garland1985] Garland, Nancy L, and David R Crosley. "Energy Transfer Processes in CH A2A and B22- in an Atmospheric Pressure Flame," 1985, 9.

[Luque2000] Luque, J, R J H Klein-Douwel, J B Jeffries, and D R Crosley. “Collisional Processes near the CH B 2Σ− v = 0, 1 Predissociation Limit in Laser-Induced FLuorescence FLame Diagnostics,” 2000, 10.

[Randall2000] Randall, Colin J, Craig Murray, and Kenneth G McKendrick. “State-Specific Collisional Coupling of the CH A 2D and B 2R— States,” 2000, 11.

[Richmond2005] Richmond, Graham, Matthew L Costen, and Kenneth G McKendrick. “Collision-Partner Dependence of Energy Transfer between the CH A2Δ and B2Σ- States,” 2005, 12.

[Kroes1993] Kroes, Geert-Jan, Ewine F van Dishoeck, and Robert A Beärda. “Photodissociation of CH2. II. Three-dimensional Wave Packet Calculations on Dissociation through the First Excited Triplet State.” *J. Chem. Phys.* 99, no. 1 (1993): 228. https://doi.org/10.1063/1.465800.

[Cameron2002] Cameron, Melanie, V Sivakumaran, Terry J Dillon, and John N Crowley. “Reaction between OH and CH3CHO.” *Phys. Chem. Chem. Phys.*, no. 4 (2002): 3628–38. https://doi.org/10.1039/b202586h.

[Sugai1990] Sugai, H, H Kojima, and A Ishida. “Spatial Distribution of CH3 and CH2 Radicals in a Methane Rf Discharge.” *Appl. Phys. Lett.* 56 (1990): 2616. https://doi.org/10.1063/1.103264.

[Jaubertau1997] Jauberteau, J L, L Thomas, J Aubreton, I Jauberteau, and A Catherinot. “High Reactivity of CH2 Radical in an AR-CH4 Post-Discharge.” *Plas. Chem. Plas. Proc.* 18, no. 1 (1997): 137.

[Yoon2002] Yoon, S F, and K H Tan. “Modeling and Analysis of Hydrogen–Methane Plasma in Electron Cyclotron Resonance Chemical Vapor Deposition of Diamond-like Carbon.” *J. Appl. Phys.* 91, no. 1 (2002): 9. https://doi.org/ 10.1063/1.1421038.

[Moeller2006] Möller, I, A Serdyuchenko, and H Soltwisch. “Analysis of the Chemistry in CH4/O2 Plasmas by Means of Absorption Spectroscopy and a Simple Numerical Model.” *J. Appl. Phys.* 100 (2006): 033302. https://doi.org/10.1063/1.2219001.

[Janev2002] Janev, R K, and D Reiter. “Collision Processes of CHy and CHy+ Hydrocarbons with Plasma Electrons and Protons.” *Physics of Plasmas* 9 (2002): 4071. https://doi.org/10.1063/1.1500735.

[Lefkowitz2015] Lefkowitz, Joseph K, Peng Guo, Aric Rousso, and Yiguang Ju. “Species and Temperature Measurements of Methane Oxidation in a Nanosecond Repetitively Pulsed Discharge.” *Phil. Trans. R. Soc. A* 373 (2015): 20140333. https://doi.org/10.1098/rsta.2014.0333.

[Togai2016] Togai, Kuninori, Nicholas Tsolas, and Richard A Yetter. “Kinetics of Plasma-Assisted Oxidation of Methane.” *54th AIAA Aerospace Sciences Meeting*, 2016. https://doi.org/10.2514/6.2016-0192.

[Balamuta1983] Balamuta, John, Michael F Golde, and Yueh-Se Ho. “Product Distributions in the Reactions of Excited Noble-gas Atoms with Hydrogen-containing Compounds.” *J. Chem. Phys.* 79 (1983): 10. https://doi.org/10.1063/1.446103.

[Pak1997] Pak, Sergei, C. Edwin Smith, Michael P. Rosynek, and Jack H. Lunsford. “Conversion of Methyl Radicals to Methanol and Formaldehyde over Vanadium Oxide Catalysts.” Journal of Catalysis 165, no. 1 (January 1, 1997): 73–79. https://doi.org/10.1006/jcat.1997.1448.

[Doebler2005] Doebler. “Oxidation of Methanol to Formaldehyde on Supported Vanadium Oxide Catalysts Compared to Gas Phase Molecules | Journal of the American Chemical Society,” 2005. https://pubs.acs.org/doi/10.1021/ja051720e.

[Feyel2007] Feyel. “Dehydrogenation of Methanol by Vanadium Oxide and Hydroxide Cluster Cations in the Gas Phase | The Journal of Physical Chemistry A,” 2007. https://pubs.acs.org/doi/10.1021/jp067454o.

[Li2010] Li, Xiang, Mei-gui Bai, Xu-mei Tao, Shu-yong Shang, Yong-xiang Yin, and Xiao-yan Dai. “Carbon Dioxide Reforming of Methane to Synthesis Gas by an Atmospheric Pressure Plasma Jet.” Journal of Fuel Chemistry and Technology, 2010, 6.

[Kim2008] Kim, Wookyung, Hyungrok Do, M. Godfrey Mungal, and Mark A. Cappelli. “Optimal Discharge Placement in Plasma-Assisted Combustion of a Methane Jet in Cross Flow.” Combustion and Flame 153, no. 4 (June 1, 2008): 603–15. https://doi.org/10.1016/j.combustflame.2007.11.015.

[Sanchez-Gonzalez2007] Sanchez-Gonzalez, Rodrigo, Yongho Kim, Louis A. Rosocha, and Sara Abbate. “Methane and Ethane Decomposition in an Atmospheric-Pressure Plasma Jet.” IEEE Transactions on Plasma Science 35, no. 6 (December 2007): 1669–76. https://doi.org/10.1109/TPS.2007.910743.

[Ohtake1990] Ohtake, Naoto, and Masanori Yoshikawa. “Diamond Film Preparation by Arc Discharge Plasma Jet Chemical Vapor Deposition in the Methane Atmosphere.” Journal of The Electrochemical Society 137, no. 2 (February 1, 1990): 717. https://doi.org/10.1149/1.2086540

[Choi2006] Choi, S. I., J. S. Nam, J. I. Kim, T. H. Hwang, J. H. Seo, and S. H. Hong. “Continuous Process of Carbon Nanotubes Synthesis by Decomposition of Methane Using an Arc-Jet Plasma.” Thin Solid Films, The Joint Meeting of 7th APCPST (Asia Pacific Conference on Plasma Science and Technology) and 17th SPSM (Symposium on Plasma Science for Materials), 506–507 (May 26, 2006): 244–49. https://doi.org/10.1016/j.tsf.2005.08.022.

[Iseni2014] Iseni, Sylvain, Stephan Reuter, Ansgar Schmidt-Bleker, and Klaus-Dieter Weltmann. “Flow and Discharge Development in an Argon Atmospheric Pressure Plasma Jet Observed by ICCD and PLIF Imaging.” IEEE Transactions on Plasma Science 42, no. 10 (October 2014): 2458–59. https://doi.org/10.1109/TPS.2014.2321226.

[Elliot2021] Elliott, Skye, and Sergey B. Leonov. “Visualization of Plasma-Assisted Mixing in a Supersonic Combustor by Acetone PLIF.” In AIAA Scitech 2021 Forum. American Institute of Aeronautics and Astronautics, 2021. https://doi.org/10.2514/6.2021-2030.

[Kee2017] R. J. Kee, F. M. Rupley, J. A. Miller, M. E. Coltrin, J. F. Grcar, E. Meeks, H. K. Moffat, A. E. Lutz, G. Dixon-Lewis, M. D. Smooke, J. Warnatz, G. H. Evans, R. S. Larson, R. E. Mitchell, L. R. Petzold, W. C. Reynolds, M. Caracotsios, W. E. Stewart, and P. Glarborg, Chemkin-Pro (Reaction Design, Inc., San Diego, CA, 2007).

[SmithGRI] G.P. Smith, D.M. Golden, M. Frenklach, N.W. Moriarty, B. Eiteneer, M. Goldenberg, C.T. Bowman, R.K. Hanson, S. Song, W.C. Gardiner, V.V. Lissianski, Z. Qin. Available from: http://combustion.berkeley.edu/gri-mech/

Appendix

A1: Profile correction

The raw PF-LIF images may contain interferences from plasma emission and LIF from CH that is naturally present in the plasma. Corrections are performed to subtract these signals from the images so that only the methyl PF-LIF signal remains. In the experiments, images were taken with all combinations of 212.8 nm and 390 nm lasers ON and OFF, resulting in a total of four images that were recorded for each point in parameter space. The labels "ON" and "OFF" are used here as shorthand notation for "unshuttered" and "shuttered" respectively. Figure A1 depicts the different images recorded during the experiment with a time delay of 1us after the last pulse in the burst. In this discussion, we will refer to the image in row *i* and column *j* of the figure as being at index (*i*,*j*). For example, the image with 390 nm OFF and 212.8 nm ON is at index (2,1). Images in the two top-most rows and two left-most columns are raw images with only the dark current subtracted. The raw PF-LIF image is at index (1,1). As can be seen, the main source of interference is the signal with the 212.8 nm laser ON and the 390 nm laser OFF, at index (2,1). Because the signal appears strongly peaked in the center of the image, which coincides with the focus of the 212.8 nm laser, this interference appears to come from a non-linear process. Interference from LIF of native CH (390 nm ON, 212.8 nm OFF) and the plasma emission (390 nm OFF, 212.8 nm OFF) contributed significantly less to the total signal. It also demonstrates the increased signal level due to the LIF laser, which was a factor of 3-4 times in this case.

Images in row 3 are obtained by subtracting images with 390 nm OFF from 390 nm ON, whereas images in column 3 are obtained by subtracting images with 212.8 nm OFF from 390 nm ON. The resulting images show the isolated effect of the 390nm laser, index (3,2), and 212.8nm laser, index (2,3) respectively. To obtain the interference corrected PF-LIF image in the plasma, S^{plasma} in Eq. 3, the corrections must account for laser generated interference and plasma emission. This correction is obtained by following the 390nm subtraction (row 3) with the 212.8 nm subtraction (column 3) and is shown at index (3,3). The final signal at (3,3) is around 75,000 counts, which is a little under half of the 160,000 counts of the raw PF-LIF image at (1,1).

The interference corrected PF-LIF image in the calibration mixture, S^{cal} in Eq. 3, is obtained in a similar way but with the addition of a third laser at 266 nm that photo-dissociates acetone to produce methyl. In principle, this correction would involve acquisition of eight images with each combination of lasers

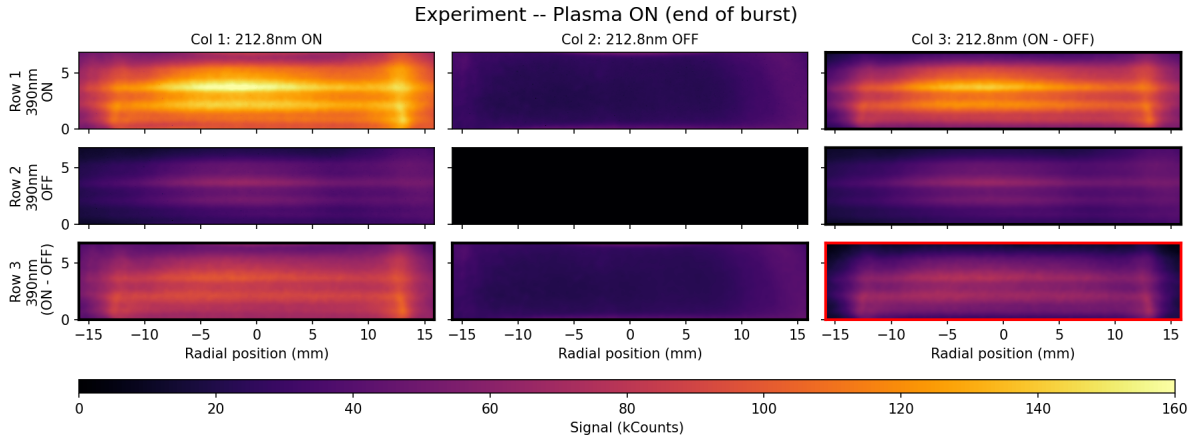

Figure A1: *PF-LIF image corrections for methyl measurements in the plane-to-plane plasma, the interference corrected plasma PF-LIF image, S^{plasma} (Eq. 3), is displayed in the bottom right corner.*

blocked and unblocked, but the signal intensities in some of these images are negligible and can be omitted. Specifically, when the 212.8 nm is OFF, no combination of the 266 nm and 390 nm lasers ON or OFF produces images with significant signal levels, so during calibration the 212.8 nm laser remains ON. The images used for calibration are shown in figure A2. The raw PF-LIF signal is depicted at index (1,1), with all three lasers ON. As observed in the plasma, the main source of interference is the signal with the 212.8 nm laser ON and the 390 nm laser OFF, at index (2,1). Even with the 266 nm beam OFF, at index (1,2), there is a non-negligible PF-LIF signal. This is likely PF-LIF of methyl produced by photolysis of acetone or methane by the 212.8 nm laser. The interference corrected calibration PF-LIF image is shown at index (3,3).

Finally, the mole fraction is determined by calculating the ratio of the interference corrected images in the plasma and the calibration, S^{plasma} (figure A1(3,3)) and S^{cal} (figure A2(3,3)) respectively, and multiplying by the methyl profile in the calibration, $x_{CH_3}^{cal}$, obtained from Eq. 1.

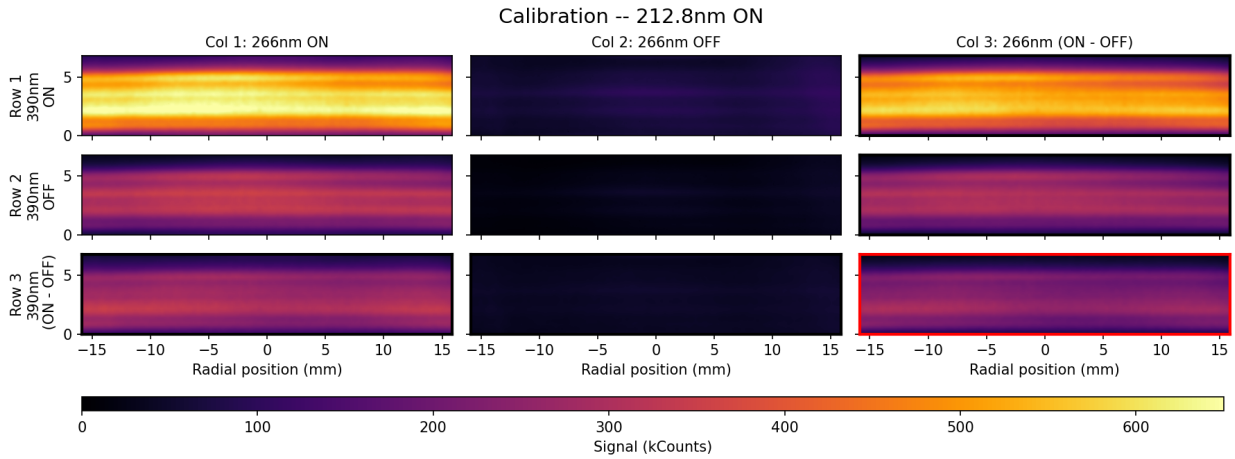

Figure A2: *PF-LIF image corrections for methyl measurements in the calibration, the interference corrected calibration PF-LIF image, S^{cal} (Eq. 3), is displayed in the bottom right corner.*